ANNALS OF GEOPHYSICS, 69, 1, S106, 2026; doi:10.4401/ag-9440
OPEN ACCESS

Application of the Vertical-to-Horizontal (VH) Ratio of the Peak Ground Velocity (PGV) in the Bay of Algiers using Data from Weak to Moderate Earthquakes

Khalissa Layadi[*,1], Fethi Semmane[1], Redouane Chimouni[1], Yacine Mohamed Tebbouche[2], Hamoud Beldjoudi[1]

(1) Astronomy, Astrophysics and Geophysics Research Center, Algiers, Algeria
(2) University of Sciences and Technology Houari Boumediene, Algiers, Algeria

Article history: received October 5, 2025; accepted January 19, 2026

Abstract

This research aims to identify the most appropriate predictor for the Vertical-to-Horizontal (VH) ratio of the Peak Ground Velocity (PGV) from the five existing models in the literature useful for regional or site-specific probabilistic seismic hazard assessment, and practical applications in the Bay of Algiers. Firstly, dataset of 285 observed VH ratios of PGV was compiled from nine seismic stations within the study area, installed on different flat and irregular surfaces. This dataset was derived from earthquakes with moment magnitude (Mw) ranging from 3.3 to 5.3. Next, the dataset was categorized into two groups based on the soil type at the station locations: rock (S1) (Vs30 above 800 m/s) and stiff (S2) (Vs30 360-800 m/s) soils. After that, a preliminary linear regression analysis was performed for each group of observed VH ratios of PGV as a function of the Joyner-Boore distance (R_{JB}) of near field and compared with three selected candidature predictors: Akkar et al. (2014), Bozorgnia and Campbell (2016), and Ramadan et al. (2021) (RA2021). For an extensive evaluation, the Euclidean Distance-based ranking method (EDR) was applied on the three mentioned candidature predictors. For rocky soil, the results indicate that all models closely align with the linear regression fit, around a VH ratio of PGV of 0.6. However, RA2021 appears to provide a reasonable fit, with a VH ratio of PGV of 0.4 for stiff soil, despite the significant site-effects at the respective stations. The EDR showed that RA2021 gives the lowest sigma with the observed ratios for S1 and S2 soil classes. For the far field, estimates of the VH ratio of PGV are provided for three strong earthquake magnitudes (6.5, 7.0, and 7.5) and different soil classes, using the existing models.

Keywords: VH ratio of PGV; predictor; soil classification; Euclidean Distance-based ranking; Bay of Algiers

1. Introduction

The destructive potential of an earthquake is estimated by its magnitude and classified according to its maximum (peak) ground-motion parameters, measured from acceleration (peak ground acceleration-PGA),

velocity (peak ground velocity-PGV), displacement (peak ground displacement-PGD), and the spectral ordinates of the response spectrum. Indeed, these parameters are mainly related to the size of the generated earthquake and the distance between the source and the site. Other factors, also, may contribute to their amplification or attenuation (e.g., soil condition, non-linearity, incidence angle, fault type, rupture directivity, etc.). In addition to their direct observation on the time series recordings, these parameters can be predicted from empirical ground motion models (EGMMs or predictors), for both horizontal and vertical components (e.g., Akkar and Bommer, 2007; Zhang et al., 2023).

In regions with an insufficient number of recorded earthquakes, a specific geology with strong local variability, or proximity to large fault ruptures, simulation-based GMMs using synthetic ground motion can provide values of ground motion comparable to those of EGMMs (e.g., Pavlenko and Pavlenko, 2021). Earthquake simulation techniques can provide an additional synthetic ground motion database to fill the gap in recorded earthquakes and construct a consistent database for generating GMMs from their combination (Anbazhagan et al., 2013). There are two main groups of simulation techniques: full waveform simulations based on real recorded events (e.g., the finite difference method; Edwards et al., 2018; Ji et al., 2025) and the stochastic simulations based on random phases (e.g., the stochastic finite-fault model; Chen et al., 2017; Karimzadeh et al., 2024).

According to Akkar and Bommer (2007), horizontal ground shaking is responsible for structural damage, but vertical ground shaking can also increase the risk of destruction. As for Chieffo et al. (2021), work on the vertical ground motion received much more attention after the recent disastrous events in central Italy, where the contribution of this motion is significant in the structural response of masonry buildings compared to horizontal motion due to its high-frequency content. Moreover, Chieffo et al. (2021) considered two scenarios on the structural capacity of masonry buildings, on the one hand, considering only horizontal ground motions and, on the other hand, considering both horizontal and vertical ground motions. They found that the vertical component significantly modified the structural capacity curve. For specific constructions, ignoring the potential of the vertical component may lead to insecure design assessments (e.g., Tsai and Lui, 2017; Ramadan et al., 2021). Indeed, Parolai et al. (2004) and Layadi et al. (2016) found that the vertical component is not always free from site-effects. Actually, the importance of vertical motion has been highlighted in the high-frequency range (5-10 Hz) and at distances close to the earthquake source (less than 15 km) (e.g., Silva, 1999; Tsai and Lui, 2017). In this case, vertical motion can exceed horizontal motion (20 % on average for rocky sites and by a factor of two for soil sites, at distances close to the source less than or equal to 5 km) (Silva, 1999).

The relationship between the horizontal and vertical components exists in both the time and frequency domains, and the ratio between them plays an important role in seismology and earthquake engineering. In this respect, the types of data used in the horizontal-to-vertical spectral ratio method are ambient vibrations and earthquakes. The results obtained are then multiple, such as the identification of the fundamental frequency (f_0) of sedimentary or topographical structures (e.g., Nakamura, 1998; Tebbouche et al., 2022; Layadi et al., 2023), soil classification (e.g., Laouami, 2020), and shear wave velocity (Vs) structure imaging (e.g., Issaadi et al., 2022; Saadi et al., 2023). On the other hand, the vertical-to-horizontal (VH) ratio plays an important role in seismic design spectra for probabilistic seismic hazard assessment. According to Ambraseys and Douglas (2003), knowledge of the relative ratio between vertical and the horizontal components allows us to quantify the contribution of the vertical component in the resistance of a building and its foundations to inertial loading. In this regard, Bommer et al. (2011) have clearly explained the need for such a ratio.

In addition to what has been mentioned above, Silva (1997) and many other studies showed that the commonly adopted VH ratio of 2/3 (Newmark and Hall, 1978) may be significantly exceeded for some conditions, such as short periods contain and the near-source distance. By way of illustration, Ramadan et al. (2021) have shown that during the 2012 earthquake in the Po Plain, a maximum VH ratio of SA was recorded in 10-14 Hz frequency range, more than 6 times, and as a function of Vs30. Indeed, the variation of VH ratio in EGMMs is mainly related to magnitude, source-to-site distance, and variations in soil condition (e.g., Ambraseys and Douglas, 2003; Bozorgnia and Campbell, 2016; Zolfaghari and Darzi, 2019; Ramadan et al., 2021; Mazloom and Assi, 2022). On their part, Ambraseys and Douglas (2003) computed the VH ratios of PGA, SA, energy density, and maximum absolute input energy as a function of earthquake surface projection, soil classification effect and focal mechanism.

The PGV is a useful parameter in earthquake engineering and seismology. As a matter of fact, Bommer and Alarcón (2006) summarized its many applications from previous studies as a potential indicator of structural damage, seismic analysis of buried pipelines, liquefaction potential, and scaling of response spectra. Specifically, Derras et al. (2020) found that the predictor of the nonlinear modulation of linear site response can be obtained from

Table 1. The available predictors for the vertical-to-horizontal (VH) ratio of PGV and their corresponding applicability in terms of magnitude (Mw), source-site distance, and ground condition.

Predictor	Databank	Mw Range	Source-to-Site Distance	Ground Condition
Gülerce et al. (2011)	Worldwide	5.0-8.5	up to 200 km	Dependent on Vs30 of the given condition in Gülerce et al. (2011)
Akkar et al. (2014) (AA2014)	Europe and Middle-East	4.0-8.0	up to 200 km	$150 \leq Vs30 \leq 1200$ m/s
Bozorgnia and Campbell (2016) (BC2016)	Worldwide	3.3-8.5	up to 300 km	Dependent on Vs30 from NEHRP soil classification (Table 2)
Zolfaghari and Darzi (2019) (ZD2019)	Dataset for Iran	4.5-7.4	up to 200 km	Iran's building design code site classification
Ramadan et al. (2021) (RA2021)	Dataset for Italy	3.5-7.5	up to 200 km	Dependent on Vs30 of the given condition in Ramadan et al. (2021)

Vs30, f_0, and the peak strain proxy PGV/Vs30. Akkar and Özen (2005), on the other hand, studied the influence of the PGV on the single-degree-of-freedom deformation demand. As for Seyhana et al. (2014) and Miura et al. (2020), they analyzed the empirical amplification of the PGV of the horizontal component with Vs30 variation, and in both studies, an inversely proportional relationship was found between PGV and Vs30. On the other side, Tsai and Lui (2017) analyzed the amplitude of the transfer function and the corresponding frequency as a function of the PGV for the horizontal and vertical components. They found that amplification is different in both directions and inversely proportional to PGV. So far, to our knowledge, there are five available VH ratio of the PGV predictors (EGMMs), which were established by Gülerce et al. (2011), Akkar et al. (2014), Bozorgnia and Campbell (2016), Zolfaghari and Darzi (2019), and Ramadan et al. (2021), using worldwide and regional datasets of small to large magnitude earthquakes (Table 1).

For Algeria, a predictor for the VH ratio of PGA and SA can be found in Laouami (2019), but there is no established predictor model for the VH ratio of PGV. In the present study, we focus on one of the Algerian cities most exposed to seismic risk, more precisely the Bay of Algiers, which constitutes our study area (Fig. 1a), in order to determine the most suitable VH ratio of PGV predictor among those presented in Table 1 for practical applications. For this purpose, we used a total number of 285 observed VH ratios of the PGV of small to moderate earthquakes presenting a good SNR (Fig. 1b) and recorded by a set of stations installed on flat and irregular surfaces (sloping terrain) in the study area (Fig. 2). Taking into account the geological, topographical, and soil classification of the site installations, our limited dataset of observed VH ratios of the PGV is categorized into three groups: (a) S1-flat rock soil, (b) S1-irregular rock soil, and (c) S2-stiff soil. S1 and S2 soil classifications are defined in the Algerian seismic design code (RPA, 2024) as shown in the Table 2.

After a first analysis of the magnitude, source-to-site distance and soil class contributions in the predictors in Table 1, we found that in the three predictors of Akkar et al. (2014), Bozorgnia and Campbell (2016), and Ramadan et al. (2021) the effect of moderate-to-low magnitude is insignificant compared with the other parameters. Based on this initial observation, the predictors in Table 1 were taken into consideration for comparison with the observed VH ratios of the PGV in each group (S1-flat rock soil, S1-irregular rock soil, and S2-stiff soil). For each group, a linear regression based on the Joyner-Boore distance, R_{JB}, was computed and compared with the results of the selected predictors. In the comparative analysis, a point-source model was considered. Then, the obtained results allowed us to select the suitable predictors for the study area.

The current work can be used for practical purposes in the study area to quantify the effect of the vertical component with respect to the horizontal component of the PGV for S1 and S2 soil classification. In addition, it can help to select predictors of the PGV's VH ratio for future seismic hazard studies, such as those already carried out in the study area (the BRGM project, 2005; the JICA project, 2006), especially for S1 and S2 soil classification. This study

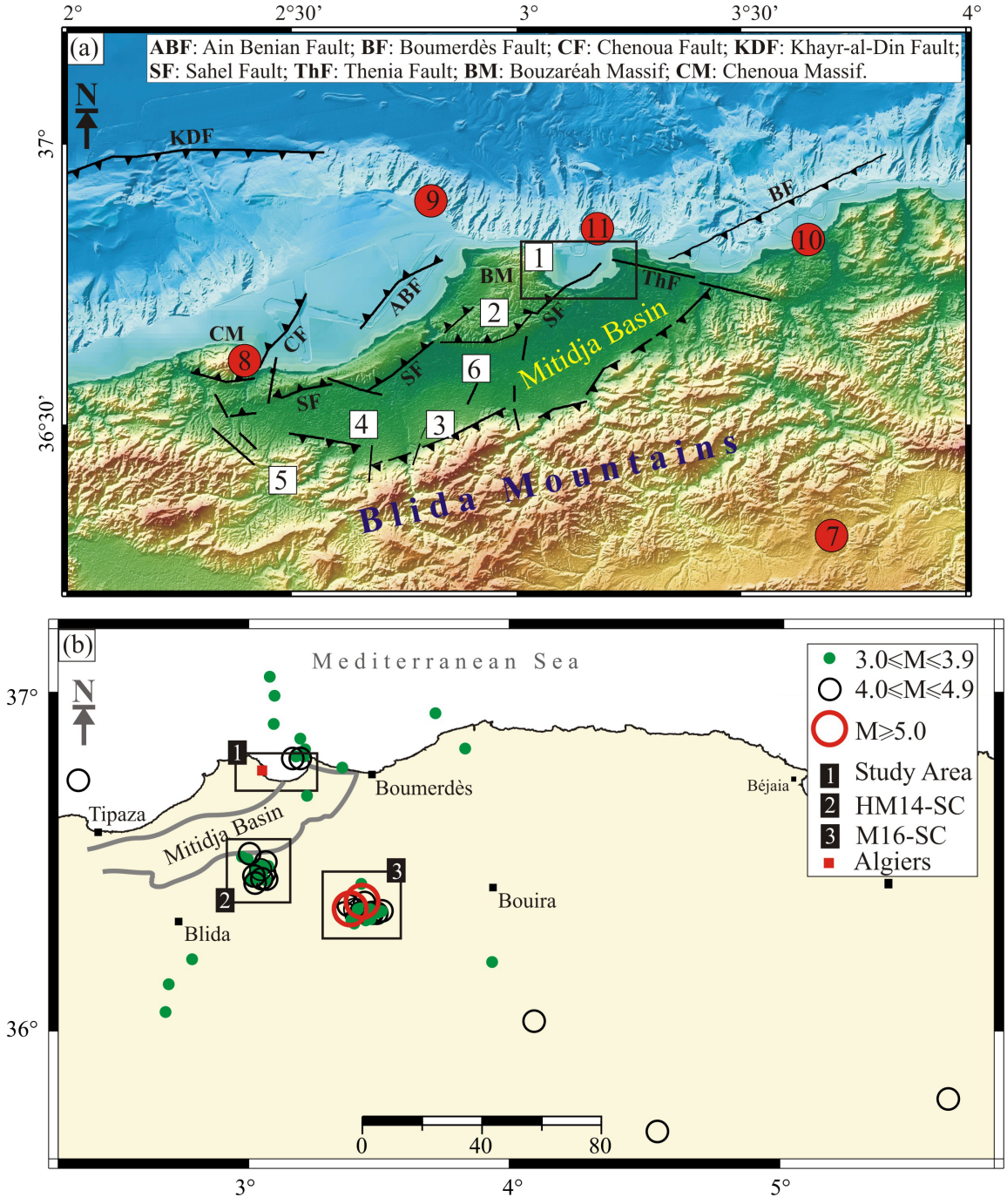

Figure 1. (a) Topographical situation of the Mitidja Basin between Blida Mountains and Bouzaréah-Chenoua Massif borders. White numbered squares and red circles are the main historical and instrumental seismic events produced in the region, respectively (see details in Table 3). Black lines with small triangles are the main active reverse faults. The black rectangle limits the study area. (b) Spatial distribution of the used earthquake data in the present study with their corresponding magnitude (details are given in Table 4). The black rectangle n° 1 limits the study area and the seismic network installation. The rectangles n° 2 and 3 limit the Hammam-Melouane-2014 (HM14-SC) and Mihoub-2016 (M16-SC) seismic crises, respectively.

quantifies the decrease in the VH ratio of PGV for S2 stiff soil caused by local amplification from lithological site effects in the horizontal component. In this study, computations of the VH ratio of PGV are provided for different soil types, earthquake magnitudes, and epicentral distances for application in engineering design or in the RPA code (2024). One can estimate vertical PGV from an observed or modeled horizontal seismic record for S1 or S2 soil types based on the VH ratios provided, and so the insights related to vertical motion can improve Algerian hazard modeling.

Table 2. Soil classification in term of Vs30 [m/s] according to NEHRP and RPA (2024).

Code	NEHRP			RPA		
Classification	Site class	Vs30	Description	Site class	Vs30	Description
	SA	>1500	Hard rock	S1	>800	Rock
	SB	760-1500	Rock with moderate weathering			
	SC	360-760	Very dense soil and soft rock	S2	360-800	Stiff
	SD	180-360	Stiff soil	S3	180-360	Soft
	SE	<180	Soft soil	S4	<180	Very soft

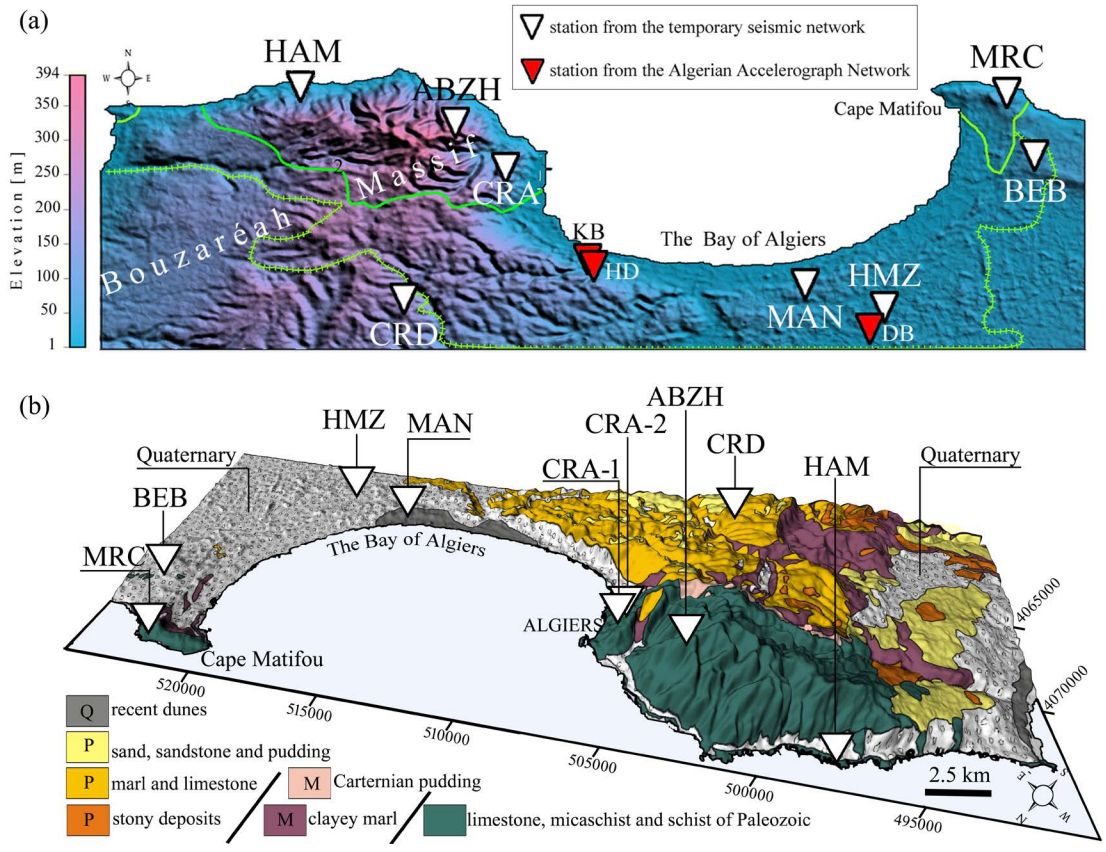

Figure 2. (a) Topographical zoom-in on the study area (black rectangle in Fig. 1a). The inverted white triangles are the stations of the temporary seismic network used in the present study and the ABZH permanent station from ADSN. The three red ones are the stations from the Algerian Accelerograph Network (operated by the CGS) of Dar-el-Beida (DB), Hussein-Dey (HD), and Kouba (KB) considered for the site-effects discussion in the present study. The continued and railroad green lines are the engineering bedrock limits from the JICA project (2006). The continued green lines limit areas with schist metamorphic rock (mi-f) engineering bedrock with Vs = 1030 m/s. The area between the continued and railroad green lines is for Plaisancian (Pliocene) marl engineering bedrock with Vs = 630 m/s. (b) The surficial geological deposits of the study area are shown on the topography of (a) for a 3D illustration, with the stations concerned by the VH ratio of PGV computations in the present study. The local geology of the study area is modified from the 1/50000 scale printed maps of the Algiers region of SGA (Service Géologique de l'Algérie).

2. Geological Context

The Bay of Algiers, our study area (Fig. 1b), is located in central northern Algeria, surrounded by numerous seismically active faults, and therefore exposed to a very high seismic risk (Fig. 1a; e.g., the JICA project, 2006; Kherroubi et al., 2009; Heddar et al., 2013; Semmane et al., 2015). Indeed, many historical and instrumental earthquakes of moderate-to-high magnitude occurred over its geological timescale (Fig. 1a, Table 3). The oldest archived seismic event near the study area was the 1365 Algiers earthquake (e.g., Maouche and Harbi, 2018), and the most recent was the 2014 Algiers earthquake (Fig. 1a, Table 3; e.g., Benfedda et al., 2017).

According to the RPA (2024), the Bay of Algiers is classified as zone IV (high seismicity zone), and in order to mitigate the seismic risk in its urban area, many microzonation projects have been carried out, such as the BRGM project (2005) and the JICA project (2006). According to the latter, the urbanization of the study area is dense and heterogeneous in terms of period and building type. The active faults shown in Fig. 1a were considered in the assessment of the seismic risk scenarios. The results obtained showed that the Chenoua and Thenia faults (CF and ThF in Fig. 1a) were able to provide a lower acceleration distribution on the rock (<3 m/s^2) than the other faults (3-6 m/s^2). Equally, consideration of the amplification factor (Midorikawa et al., 1994) showed that the highest acceleration (over 8 m/s^2) from the Boumerdès Fault can be recorded in the area between stations BEB, HMZ, and MAN (Fig. 2a), becoming more significant towards the south. In addition, many potentially induced phenomena were presented by the JICA project (2006) in the form of hazard maps for liquefaction and slop stability (Hallal et al., 2019).

After the 2003 Boumerdès earthquake, studies on site-effects in the Bay of Algiers and the Mitidja Basin, in general, were intensified using experimental techniques and numerical modeling for better characterization of ground response (e.g., Gherboudj et al., 2024a), soil frequency identification (e.g., Meslem et al., 2010; Tebbouche et al., 2017), and soil classification (Laouami, 2020). Accordingly, using numerical modeling, site-effects in the Bay of Algiers were estimated in the BRGM project (2005) and the JICA project (2006), considering the contributions of the sediment layer and topography in the site response and amplification factor assessments.

From the topographical point of view, the Bay of Algiers occupies flat and irregular surfaces (sloping terrain) compared to sea level, as shown in the 3D illustration in Fig. 2b. In effect, the flat surface is part of the Mitidja Basin, and

Table 3. Main historical (n° 1 to 6 in Fig. 1a) and instrumental (n° 7 to 11 in Fig. 1a) earthquakes occurred in the Mitidja Basin and surrounding area (Fig. 1a).

N°	Earthquake Name	Year/Mt./Day	Lat-Lon [°]	I_0	M
1	Algiers	1365/1/3	36.8-3.05	X	
2	Algiers	1716/2/ 3	36.7-2.95	IX	
3	Blida	1825/ 3/2	36.5-2.83	IX	
4	Mouzaia-El Affroun	1867/1/2	36.5-2.66	IX	
5	Aumale	1910/6/24	36.3-3.70	VIII	6.4
6	Douéra	1924/11/5	36.6-2.91	VIII	5.2
7	Bou Medfaa	1959/11/7	36.4-2.48	VIII	5.1
8	Chenoua	1989/10/29	36.57-2.32	VIII	6.0
9	Ain Benian	1996/ 9/ 4	36.90-2.81		5.7
10	Boumerdès	2003/5/21	36.83-3.65	X	6.8
11	Algiers	2014/ 8/1	36.85-3.18	VII	5.5

the sloping terrain is represented by the Bouzaréah Massif, oriented east-west, whose highest point is 394 m (Fig. 2a). Also, the local geology of the study area is shown in Fig. 2b. The geological deposits originate from four system periods: Quaternary, Pliocene, Miocene, and Paleozoic, depending on whether we are on the plain (Quaternary) or at altitude (the other deposits). The Quaternary deposits of the Mitidja Basin and recent sand dunes are mainly cover the flat surface (e.g., Derrich and Cheikh-Lounis, 2004). The sloping terrain of the Bouzaréah Massif is covered by Pliocene and Miocene sands, sandstones, limestones, and marls overlying the metamorphosed Paleozoic rock of the massif (Fig. 2b).

According to Layadi et al. (2023), the seismic bedrock of the study area is the metamorphosed Paleozoic rock outcropping in the Bouzaréah Massif and at Cape Matifou in the inner zone of the crystalline massifs of northern Algeria, composed mainly of schist and gneiss with some local deposits of Bouzaréah limestone (Fig. 2b). For Derrich and Cheikh-Lounis (2004), the Plaisancian (Pliocene) marl forms an engineering bedrock; however, it was determined that a Vs = 630 m/s for this geological deposit by the JICA project (2006). Consequently, for the study area, the JICA project (2006) defined another metamorphic schist engineering bedrock with a Vs = 1030 m/s. Figure 2a shows the limits of these two engineering bedrocks, modified from the JICA project (2006) map. Basing on the compilation and interpolation of available boreholes, the JICA project (2006) proposed maps showing the variation in thickness of sediment layers in the study area overlying the bedrock. The maximum was found to be 200 m of Plaisancian (Pliocene) marl, south of the HMZ station.

3. Data and Seismic Network

In the present study, we used seismic events recorded by a temporary seismic network of eight three-component seismic stations (Fig. 1b and 2b, Table 4) and the Algerian Digital Seismic Network (ADSN) ABZH permanent station (Yelles-Chaouche et al., 2013; Layadi et al., 2023). The stations are located at different geomorphological sites in the study area (in Fig. 2b). The temporary seismic network stations were installed from August 2014 to October 2016, recording seismic events from three nearby seismic sequences: 2014 Hammam-Melouane; 2014 Algiers (Yelles-Chaouche et al., 2018); 2014 Mihoub (Semmane et al., 2017); and 2016 Mihoub (Khelif et al., 2018) earthquake sequences (Fig. 1b).

More precisely, the stations were located respectively in the Bouzaréah Massif (ABZH, CRA-1, CRA-2, CRD, and HAM), the eastern part of the Mitidja Basin (BEB, HMZ, and MAN), and the flat rock of Cape Matifou (MRC) (Fig. 2b). In fact, the stations (BEB, CRA-1, CRA-2, CRD, HMZ, HAM, MAN, and MRC) were equipped by the L22 Mark Products (fc = 2 Hz) and broadband STS2 (ABZH) sensors. The used sampling rates were 100 sps (CUBE3 and QUANTERRA Q330 digitizers) and 75 sps (GEOSTAR digitizer). From a geological point of view, the stations BEB, HMZ, and MAN, were located on flat Quaternary sediments (Fig. 2b). The ABZH CRA-1, CRA-2 stations are located on irregular hard rock, the MRC station was installed on flat hard rock, and stations CRD, and HAM were installed on irregular sediment layers overlying the hard rock of the Bouzaréah Massif (Fig. 2b). The JICA project (2006) proposed a map to show limits of the two types of engineering bedrocks (Fig. 2a), Plaisancian (Pliocene) marl with Vs = 630 m/s, and schistose metamorphic rock with Vs = 1030 m/s. Based on this mapping, the nature of the engineering bedrock beneath each station is presented in Table 5. This bedrock identification is useful in explaining the origin of site-effects in the study area.

In the present study, the dataset consists of seismic events with moment magnitudes (Mw) ranging from 3.3 to 5.3 with signal-to-noise ratio (SNR) being higher than three in the frequency domain from 0.1 to 10 Hz of engineering interest. In this study, two SNR criteria were applied, the first is the frequency-amplitude plot of Clinton and Heaton (2002) for the seismic dataset of near and far fields, with different magnitude classes (M1.5, M2.5, M3.5, M4.5…). In this criterion, our seismic events of M2.5, and M3.5 of regional earthquakes were automatically eliminated because the spectral amplitude is drowned out in Peterson's (1993) model. Then, we applied the second SNR criterion to the remaining seismic events, which consists of calculating the individual spectral ratios between the seismic signal amplitudes and the corresponding pre-event ambient noise using the Fast Fourier Transform (FFT), smoothed using the Konno-Ohmachi algorithm with a smoothing constant of 40 (Konno and Ohmachi, 1998). Seismic events with SNRs higher than three in the frequency domain from 0.1 to 10 Hz were selected to build our seismic dataset. Details of the seismic events of our dataset are presented in Table 4. The data used contain mainshocks, some of their aftershocks, and independent events (Fig. 1b). For the conversion of the magnitude Md given by the CRAAG catalog, we used the conversion expression of Roubeche (2025).

Table 4. Used earthquake data in the present study recorded by the stations of the temporary seismic network installed in the study area (Fig. 2b) and ABZH with their date, origin time, localization, magnitude, Md, and depth, Z, from the CRAAG catalog.

N°	Year	Mot.	Day	Hour	Mnt.	Long (°)	Lat (°)	M	Z (km)	ABZH	BEB	CRA-1	CRA-2	CRD	HAM	HMZ	MAN	MRC
1	2014	8	1	4	26.69	3.206	36.812	4.7	6.47	●								
2	2014	8	7	20	32.49	3.106	36.915	3.4	17.9			●						●
3	2014	8	9	10	19.73	3.2	36.811	4.0	3.35	●					●			
4	2014	9	6	8	50.65	3.205	36.871	3.4	4.44	●					●			
5	2014	9	8	11	46.32	3.057	36.477	4.0	9.33		●				●			●
6	2014	10	10	9	02.70	3.061	36.465	3.7	8.26					●	●	●	●	●
7	2014	11	15	1	12.98	3.445	36.378	4.4	6.84			●		●		●	●	●
8	2014	11	15	19	43.90	3.408	36.357	4.1	9.86			●		●		●	●	●
9	2014	11	27	22	10.30	3.063	36.489	3.6	6.76			●			●	●	●	●
10	2014	12	16	15	02.56	3.05	36.466	3.6	6.99			●		●	●	●	●	●
11	2014	12	19	11	06.06	3.016	36.525	4.7	4.97		●	●		●	●	●	●	●
12	2014	12	19	11	12.64	3.057	36.474	3.9	7.1			●		●	●	●	●	●
13	2014	12	20	10	29.79	3.029	36.461	3.1	8.02						●			
14	2014	12	20	18	31.38	3.048	36.474	3.5	8.37					●	●			
15	2014	12	21	17	53.92	3.045	36.454	3.6	7.65			●		●	●	●	●	●
16	2014	12	23	6	33.26	3.039	36.487	3.3	6.12					●		●		●
17	2014	12	23	8	00.35	3.032	36.458	4.9	8.4	●	●			●		●	●	●
18	2014	12	23	8	33.64	3.009	36.508	3.4	8.48	●		●			●	●	●	●

N°	Year	Mot.	Day	Hour	Mnt.	Long (°)	Lat (°)	M	Z (km)	ABZH	BEB	CRA-1	CRA-2	CRD	HAM	HMZ	MAN	MRC
19	2014	12	23	8	59.04	3.062	36.45	4.7	2.23	●	●	●		●	●	●	●	●
20	2014	12	26	17	55.27	3.079	36.448	4.4	7.8		●					●	●	●
21	2015	1	1	14	17.18	3.71	36.947	3.7	4.58							●		
22	2015	2	1	20	06.57	3.072	36.467	4.5	6.76	●	●			●		●	●	●
23	2015	2	21	12	53.31	3.026	36.449	3.1	8.08					●				
24	2015	3	16	11	13.16	3.037	36.436	4.1	12.07					●	●	●	●	●
25	2015	3	16	11	37.39	3.021	36.443	3.7	7.51					●	●	●	●	●
26	2015	3	21	22	55.92	5.628	35.783	4.8	4.44	●	●					●		
27	2015	3	23	1	58.35	3.047	36.475	3.3	15.70						●			
28	2015	3	28	7	34.16	3.091	37.056	3.6	13.24						●			●
29	2015	3	28	10	22.18	3.109	37	3.4	19.4						●			●
30	2015	4	4	12	27.59	3.077	36.445	3.4	5.99	●				●	●	●	●	●
31	2015	4	28	17	27.61	3.189	36.817	3.7	5.09								●	●
32	2015	7	11	14	25.81	2.801	36.206	3.9	9.45						●	●		●
33	2015	7	15	7	38.77	4.54	35.684	4.2	8.75	●								
34	2015	8	21	1	10.99	3.218	36.818	3.3	6.28						●		●	
35	2015	8	25	9	58.38	3.821	36.841	3.9	6.23							●	●	●
36	2015	10	23	14	48.57	3.363	36.784	3.1	9.87							●		
37	2015	11	16	7	13.44	3.045	36.462	3.1	8.16						●			
38	2015	11	21	3	18.94	2.987	36.516	3.0	1.74							●		

N°	Year	Mot.	Day	Hour	Mnt.	Long (°)	Lat (°)	M	Z (km)	ABZH	BEB	CRA-1	CRA-2	CRD	HAM	HMZ	MAN	MRC
39	2015	12	17	21	20.77	3.23	36.7	3.1	7.03		●				●		●	●
40	2016	2	10	1	12.23	3.077	36.5	4.7	9.95	●	●				●	●	●	●
41	2016	3	24	8	06.26	3.385	36.369	4.1	4.02	●	●			●	●		●	●
42	2016	3	29	13	25.20	2.713	36.131	3.7	10.5	●					●			
43	2016	4	10	17	48.86	3.392	36.359	5.0	5.86	●	●			●	●	●	●	●
44	2016	4	10	21	23.50	3.393	36.336	3.0	4.80						●	●	●	
45	2016	4	11	11	40.98	3.397	36.325	3.6	14.13		●				●	●		●
46	2016	4	13	6	20.89	3.452	36.344	3.4	11.8	●	●				●		●	●
47	2016	4	16	4	27.34	3.464	36.353	3.6	6.92	●	●			●				●
48	2016	4	21	13	32.18	3.457	36.331	3.7	10.08	●	●					●	●	●
49	2016	5	16	9	19.04	3.476	36.343	4.7	4.61	●	●			●			●	●
50	2016	5	16	20	07.61	3.467	36.357	3.9	4.61	●	●						●	●
51	2016	5	28	23	54.91	3.436	36.382	5.3	6.96	●				●				●
52	2016	5	29	1	54.74	3.434	36.434	3.5	5.72								●	
53	2016	5	29	4	09.27	3.414	36.357	3.5	8.18	●	●			●			●	●
54	2016	5	29	5	23.17	3.371	36.347	4.0	2.85	●	●			●			●	●
55	2016	5	29	13	17.98	3.42	36.357	3.8	1.53	●	●		●			●	●	
56	2016	5	29	23	05.74	3.473	36.348	4.1	5.62	●	●		●	●			●	●
57	2016	5	30	12	08.70	3.418	36.337	3.4	1.52		●							

N°	Year	Mot.	Day	Hour	Mnt.	Long (°)	Lat (°)	M	Z (km)	ABZH	BEB	CRA-1	CRA-2	CRD	HAM	HMZ	MAN	MRC
58	2016	5	30	16	44.11	3.438	36.33	3.2	7.81	●	●							
59	2016	5	31	6	13.05	3.428	36.347	3.3	4.74	●	●							
60	2016	5	31	17	35.20	3.431	36.348	4.5	7.26	●	●		●	●			●	●
61	2016	5	31	20	09.01	3.511	36.352	3.5	1.22	●								●
62	2016	5	31	23	05.10	3.426	36.33	3.4	7.23									●
63	2016	6	1	6	02.17	3.45	36.324	3.3	13.44		●							
64	2016	6	1	9	12.34	3.468	36.339	3.5	5.87	●								
65	2016	6	1	22	34.29	3.422	36.355	4.1	6.36	●	●		●	●	●		●	●
66	2016	6	4	3	53.12	3.407	36.314	3.8	14.56	●	●		●		●		●	
67	2016	6	4	5	21.35	3.492	36.346	4.1	6.81	●	●		●	●	●		●	●
68	2016	6	11	22	57.90	2.376	36.746	4.0	7.74		●		●		●		●	●
69	2016	6	11	23	58.63	3.494	36.347	3.6	6.11		●		●	●	●		●	●
70	2016	6	14	19	00.46	3.923	36.198	3.8	7.05	●	●						●	●
71	2016	7	6	20	52.46	3.51	36.353	4.1	6.62				●		●	●	●	●
72	2016	9	8	1	42.71	3.085	36.488	3.5	7.85	●	●		●	●	●	●	●	●
73	2016	9	20	19	23.40	3.223	36.839	3.7	5.68		●			●		●	●	●
74	2016	10	8	10	38.72	3.467	36.327	3.6	8.4		●							●
75	2016	10	9	23	03.70	2.701	36.046	3.9	12.3	●				●				●
76	2016	11	5	20	43.37	4.080	36.019	4.7	9.23	●								

4. Analysis

4.1 HVSRN technique

To get an early view of the site response at each station from the seismic network, we applied the Nakamura technique (or the Horizontal over Vertical Spectral Ratio using ambient Noise, HVSRN, technique; Nakamura, 1989) using the GEOPSY Open-Source Tool Set (Wathelet et al., 2020) to analyze ambient vibration data and calculate experimental curves. For each station, one hour of ambient vibrations for the three components, EW, NS, and V, was selected in the quiet period, then from the automatic window selection in the GEOPSY software, we used 50 sec time windows (SESAME, 2004). In our processing, we used the following filtering parameters, STA = 1.0 sec, LTA = 30 sec, with minimum and maximum ratio STA/ LTA of 0.20 and 2.5, respectively. These selections are default values proposed by GEOPSY, which fall within the range of windows recommended by the SESAME guide (2004). The Fast Fourier Transform of the time windows was calculated between 0.1 and 20 Hz and smoothed using the Konno-Ohmachi algorithm with a smoothing constant of 40 (Konno and Ohmachi, 1998). Individual HVSRNs were calculated by dividing the quadratic mean of the horizontal Fourier spectra by the vertical one, then an average HVSRN was calculated with minimum and maximum curves.

4.2 Observed VH ratios of the PGV

Before calculating the observed VH ratios of the PGV from our seismic event set, for each event i recorded by station j, a pre-processing was performed on the 3 components of the seismic recordings, removing the mean, the trend, and the instrumental response. Although no formal error propagation was performed, the uncertainty associated with PGV measurements is mainly related to instrumental noise and signal processing choices. These sources of uncertainty were mitigated by using well-calibrated sensors and a uniform processing workflow for all events.

The absolute maximum values of the 3 components on each seismic signal record were saved as PGV_{EW_ij}, PGV_{NS_ij} and PGV_{V_ij}. After calculating the ratios between the PGVs of horizontal components such as PGV_{EW_ij}/PGV_{NS_ij}, we found that the majority have a variation around unity (between 0.75 and 1.25). Building on this result, a mean horizontal component (quadratic mean), PGV_H, was calculated for each event recorded by each station using the Eq. (1). Next, the individual VH ratios of the PGV were calculated between PGV_{V_ij} and the corresponding average PGV_{H_ij} as $(VH)_{ij} = PGV_{V\_ij}/PGV_{H\_ij}$.

$$PGV_{H_{ij}} = \sqrt{\left(PGV_{EW_{ij}}^2 + PGV_{NS_{ij}}^2\right)/2} \tag{1}$$

4.3 Soil classification of the seismic stations

The soil classification step of the seismic stations is necessary for a comparison and selection of VH ratio of the PGV predictors from Table 1. Here, we used two approaches, the map of soil classification of Gherboudj et al. (2024a) and the classification of Laouami (2020) based on the H/V target spectral ratio computation using ambient vibrations. At this level, the soil classifications in the two approaches are defined from RPA (2024), based on Vs30 (Table 2). The special distribution of the soil classification of Gherboudj et al. (2024a) is based on the geological units, geotechnical soil models, and geophysical investigations, available in the study area. In the application of the approach of Laouami (2020) in the present study, we used the same ambient vibrations dataset in HVSRN technique for all stations except ABZH, CRA-1, and CRA-2 sites affected by the topographic site-effects according to Layadi et al. (2022 and 2023).

The soil classification of Gherboudj et al. (2024a) and Laouami (2020) showed a good agreement for BEB and HMZ stations with S2 (stiff soil) and CRA-1, CRA-2, CRD, HAM, and MRC sites with S1; however, for MAN stations, a difference in soil classification was obtained (Table 5). Thus, the soil classification of ABZH, CRA-1, and CRA-2 stations are defined as S1 from its local geology in Fig. 2b as schist metamorphic rock, in agreement with Gherboudj et al. (2024a).

The final soil classification used in the present study is given in column n°5 of Table 5 of each station based on the results of the Laouami (2020) approach and the geological units of rocky site installations. The seismic stations were grouped into two soil classes, S1 (rocky soil) and S2 (stiff soil). The S1class includes stations CRA-1, CRA-2, CRD, HAM, MAN, and MRC, and the class S2 includes stations BEB and HMZ (Table 5). The magnitude-epicenter distance of the used earthquakes is plotted in Fig. 3a as a function of the corresponding soil classification, S1 and S2. Figure 3a shows that the most frequently used seismic events have epicentral distances of less than 75 km and are mainly recorded by stations of S1 soil classification.

4.4 Observed VH ratios of the PGV versus soil classification

In Fig. 3b, the distribution of all observed VH ratios of the PGV is shown as a function of Mw and soil classification. In Fig. 3c and 3d, histograms of each soil class, S1 and S2, respectively, are plotted, showing the number of observed VH ratios of the PGV in different intervals. The total number of VH ratios of the PGV in S1 class (rocky soil) is 218 for stations ABZH, CRA-1, CRA-2, CRD, HAM, MAN, and MRC, and 67 in S2 class (stiff soil) for stations BEB and HMZ stations (Table 5, Fig. 2b). In Fig. 3c, there are no VH ratios of the PGV below 0.2 in S1, and in Fig. 3d there are no VH ratios of the PGV above 1.0 for S2. Furthermore, for S1 soil classification (rocky soil), we made a separation on the observed VH ratios of the PGV considering the topography of the site installation, as flat and irregular surfaces (sloping terrain). As a result, this operation gave rise to two categories: S1-flat includes the MRC and MAN stations, and S1-irregular includes the stations ABZH, CRA-1, CRA-2, CRD, and HAM installed in the Bouzaréah massif.

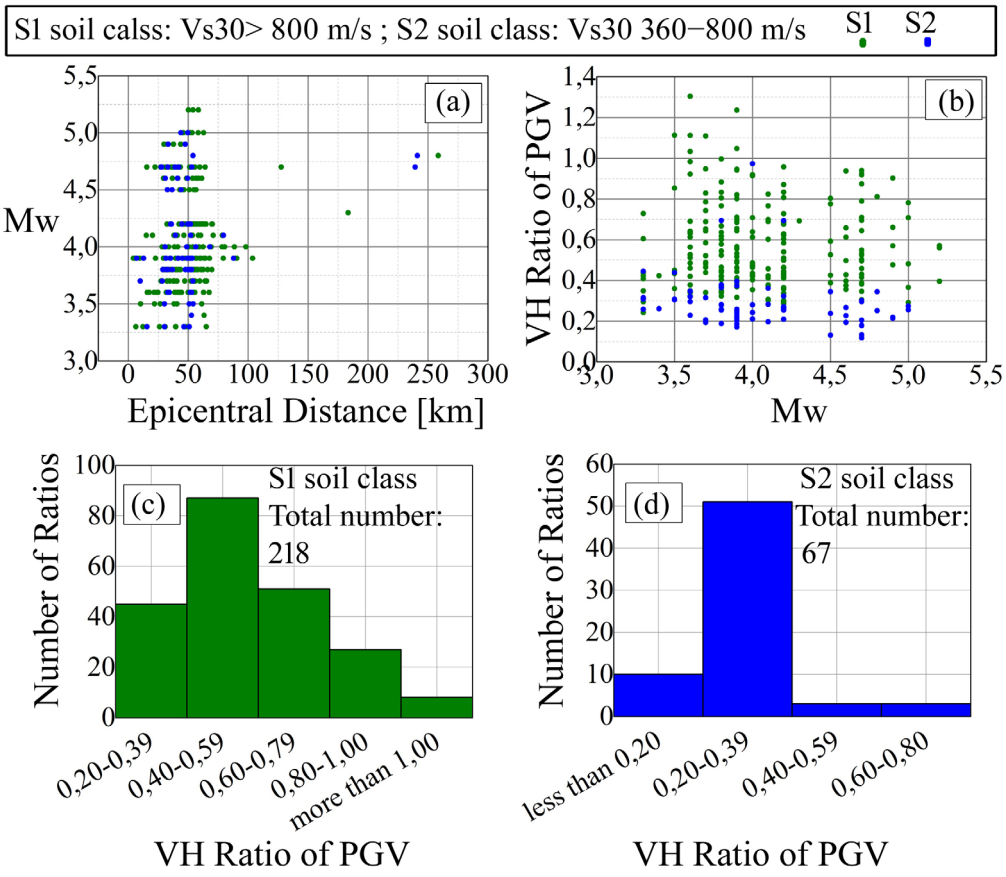

Figure 3. (a) Mw magnitude of seismic events of Table 4 distributed as a function of Epicentral distance and soil classification (S1 in green and S2 in blue) of the seismic stations in Table 5. In (b) it is shown the variation with Mw of the observed VH ratios of PGV from the seismic dataset in (a) and the corresponding soil classification. In (c) and (d) histograms showing the number of VH ratios of PGV for each soil classification, S1 (in green) and S2 (in blue), using variations in intervals.

Table 5. Engineering bedrock beneath each station in Fig. 2b, according to the JICA project (2006) (EB-JICA06). In the case of CRD station, we accompanied the bedrock with (!), since we based only on the geological maps. The soil classification of the stations are given according to Gherboudj et al. (2024) (GH24) and Laouami (2020) (LA20) approaches using the Algerian seismic design definition in Table 2 (RPA, 2024). The ABZH, CRA-1, and CRA-2 stations were expected in soil classification using the LA20 approach since the identified f_0 is caused by topographic site-effects (Layadi et al., 2022 and 2023). In column n° 5 (Soil Classification), it is given the soil classification used in the present study. The f_0 from HVSRN technique and the corresponding origin are given in column n° 6 and 7, respectively.

Station	EB-JICA06	GH24	LA20	Soil Classification	f_0 [Hz]	Site-Effects Origin
ABZH	mi-f	S1	—	S1	3	topographic
BEB	p-f	S2	S2	S2	2.5	lithological
CRA-1	mi-f	S1	—	S1	12.5	topographic
CRA-2	mi-f	S1	—	S1	9	topographic
CRD	p-f (!)	S1	S1	S1	broad-peak	atypical
HAM	mi-f	S1	—	S1	8	topographic
HMZ	p-f	S2	S2	S2	4.5	lithological
MAN	p-f	S2	S1	S1	non-flat curve	unclear
MRC	mi-f	S1	S1	S1	flat	reference site

p-f: Plaisancian (Pliocene) marl; mi-f: schist metamorphic rock.

4.5 Selection of VH ratio of the PGV predictors

In our comparative analysis for a selection of the most suitable VH ratio of PGV predictors from Table 1, we first examined their Mw range in relation to our database in Fig. 3a. We found that the Gülerce et al. (2011) predictor cannot be considered in the present study, as the model is useful for Mw ≥ 5. In Fig. 4, the VH ratio of PGV variation with Mw are plotted for predictors AA2014, BC2016, ZD2019, and RA2021 from Table 1, taking into account soil classification (rock, stiff, and soft). The Mw variation band was selected from the lower limit of the corresponding predictor according to Table 1 with a step size of 0.2 up to 5.9 for predictors BC2016, ZD2019, and RA2021, and up to 6.0 for predictor AA2014. In our computation of the modeled VH ratio of PGV from the four mentioned predictors, six R_{JB} values were used: 1, 5, 10, 30, 50, and 100 km. After comparing the results obtained, we illustrated the modeled VH ratios of PGV for 5, 30, and 100 km only for convenience. In the application of soil classification in the four predictors, we considered three classes: rocky soil with Vs30 = 1030 m/s, stiff soil with Vs30 = 500 km, and soft soil with Vs30 = 250 m/s. Concerning the application of the BC2016 predictor, we used the technical guide by Kaklamanos et al. (2011) and the corresponding software for RRUP to R_{JB} conversion.

Figure 4 shows that for the AA2014, BC2016, and RA2021 predictors, soil conditions play the major role in the variation of the modeled VH ratio of PGV compared to the ZD2019 predictor, for which the most important influence comes from the variation of R_{JB}. In the ZD2019 predictor, the variation of the VH ratio of PGV is very small when the soil class changes from rock to stiff and soft, compared to the variations observed in other predictors and in our input database of observed VH ratios of PGV (Figs. 3c and 3d and 4). This limited variation does not align with the specific aim of our study, which treats soil classification as a key parameter in the comparative analysis. Consequently, the ZD2019 predictor was excluded from the final comparisons.

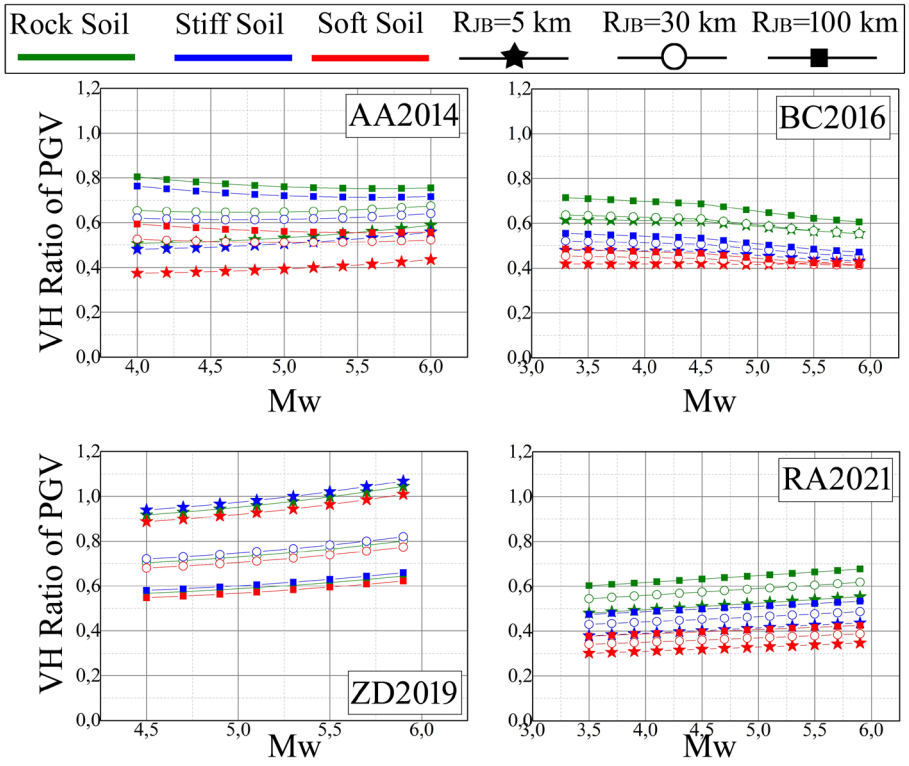

Figure 4. Mean modeled VH ratio of PGV variations with moment magnitude, Mw, and Joyner-Boore distance, R_{JB}, of 5, 30, and 100 km, estimated from the prediction of Akkar et al. (2014) (AA2014), Bozorgnia and Campbell (2016) (BC2016), Ramadan et al. (2021) (RA2021), and Zolfaghari and Darzi (2019) (DZ2019), for rock (Vs30 = 1030 m/s), stiff (Vs30 = 500 m/s), and soft (Vs30 = 250 m/s) soils. In the four predictors, the reverse fault type was considered.

According to Fig. 4, near and far fields have an influence on the VH ratio of PGV, mainly in the ZD2019 predictor. For the other predictors, a much weaker influence is observed, with soil class playing a major role in its variation. For example, for rocky soil, when Mw = 5.0 and R_{JB} = 30 and 100 km, the variation in the VH ratio of PGV is less than 0.1 for the AA2014, BC2016 and RA2021 predictors.

There is a notable difference between the VH ratios of PGV variation obtained from the AA2014, BC2016, and RA2021 predictors, as shown in Fig. 4, for the same R_{JB} value and soil class. For example, for a stiff soil class and an R_{JB} set at 100 km, AA2014 provides a VH ratio of PGV of around 0.7, while the BC2016 and RA2021 predictors provide a VH ratio of PGV of around 0.5. This difference between predictors is due to many parameters, such as differences in regional soil profiles, wave propagation effects, or insufficient parameterization of the site response in these models. Regarding the latter point, Bozorgnia and Campbell (2016) (BC2016) used two different site response functions: shallow site response and basin response. Ramadan et al. (2021) used a linear site response function, while Akkar et al. (2014) used a non-linear function.

The AA2014, BC2016, and RA2021 predictors showed that the effect of Mw on the VH ratio of PGV relative to R_{JB} is very small. For example, using the BC2016 predictor for rocky soil, with an R_{JB} = 100 km and Mw = 3.5, 4.5, and 5.5, the VH ratios of PGV are 0.71, 0.69, and 0.62, respectively (Fig. 4). For the same soil classification, an R_{JB} distance (100 km) and a magnitude Mw = 4.6 and 5.6 in the AA2014 predictor, the VH ratios of PGV are equal to 0.77 and 0.75, respectively. For a stiff soil, R_{JB} = 100 km, and Mw = 3.5, 4.5, and 5.5 in the RA2021 predictor application, the VH ratios of PGV are equal to 0.48, 0.50, and 0.52, respectively (Fig. 4). The effect of magnitude on VH ratios of PGV becomes smaller for R_{JB} below 100 km (Fig. 4). Based on this result, in our comparative analysis with the limited dataset of 285 observed VH ratios of PGV, we neglected the effect of the magnitude variation and kept only the variations in R_{JB} and soil classification.

Here, we considered the AA2014, BC2016, and RA2021 predictors for the two soil classes in Table 5, S1 (rocky soil) with Vs30 = 1030 m/s based on JICA (2006) bedrock mapping, and S2 (stiff soil) with an average of Vs30 = 400 m/s. For the conversion of epicentral distance to R_{JB} in our approximation case, we considered a point-source model where the epicentral distance = R_{JB}. In the present study, we used a seismic database of weak to moderate earthquakes (Fig. 3a),

so the approximation of the point-source model is valid. In contrast, this model is not applicable for large earthquakes case, because the fault rupture length can be tens to hundreds, leading to significant differences between hypocentral distance and fault-to-site distance (Atkinson and Boore, 2009; Xiao and Yamada, 2022). The number of observed far-field VH ratios of PGV is limited (only 10 ratios) compared to near-field data (275 ratios) (Fig. 3a; an 80 km limit was used according to Campbell and Bozorgnia, 2014). Therefore, we only considered observed VH ratios of PGV with epicentral distances less than 75 km (Fig. 3a). Based on these steps, three preliminary linear fittings were calculated from the observed VH ratios of PGV of S1-flat surface, S1-irregular surface, and S2.

5. Results and Discussion

The first result of the present study consists of response curves for the station sites using the HVSRN technique, as shown in Fig. 5. The HVSRN curves are plotted in the frequency domain from 0.1 to 20 Hz for a better illustration of the frequency peaks with the corresponding troughs (or zero, fz $\sim 2 * f_0$). For example, at BEB, CRA-1, and HAM sites, the corresponding fz are at 12, 20, and 15 Hz respectively (Fig. 5). Indeed, all stations show a clear f_0 in the high (BEB, CRA-1, CRA-2, HAM, and HMZ), and a broad peak at the ABZH and CRD stations, as well as irregular or non-flat responses (MAN), with the exception of station MRC, which presents a flat curve. The corresponding f_0 variation to each case is presented in Fig. 5 in the intervals between the minimum and maximum values. To validate the identified frequency peaks, we considered the criteria of the SESAME guide (2004) for reliable curves and clear peaks, based on many parameters, such f_0, A_0, the corresponding standard deviations, the window length, the number of windows, etc. Applying these criteria to our HVSRN curves and f_0 yielded very satisfactory results. In an article currently under submission, we presented an analysis of the origin of site-effects at the site installations shown in Fig. 2b, using multi-method approaches, where more details, computations, and interpretations are provided.

The second result of the present work is the observed VH ratios of PGV presented as a function of the variations in epicentral distance (Fig. 6) and azimuth (Fig. 7) for each station in Fig. 2b, categorized according to three classes of Mw: 3.0-3.9, 4.0-4.9, and 5.0-5.9. In Fig. 6, only ABZH, BEB, and HMZ stations recorded few seismic events with epicentral distances greater than 100 km. In the interval 0-100 km, the first observation we can make is that VH

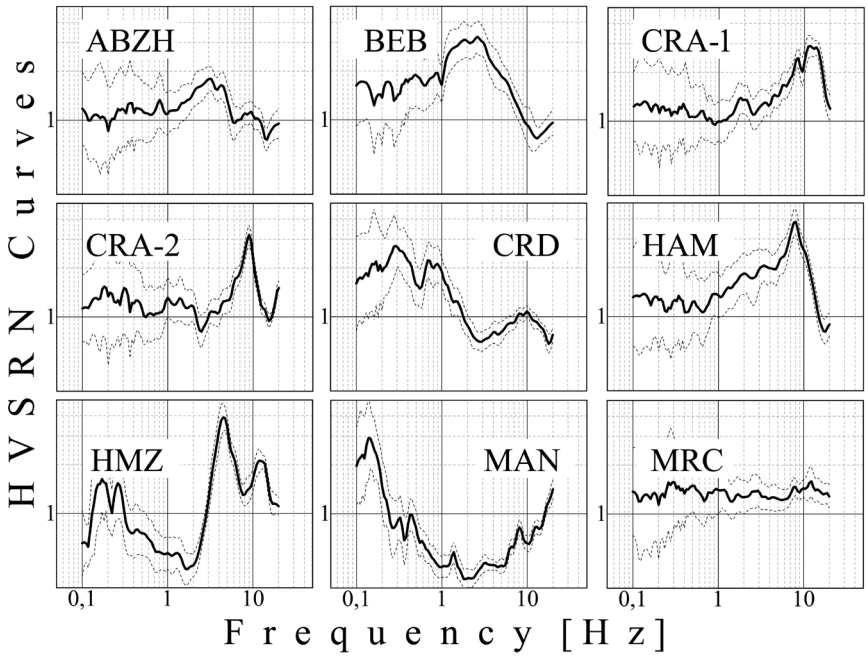

Figure 5. The HVSRN curves (solid lines) of the considered seismic stations in Fig. 2b using the 40 b-values of the Konno-Omachi smoothing algorithm (Konno and Omachi, 1998), with the corresponding clear fundamental frequency, f_0, ± min and max values in yellow rectangles. Thin dashed lines are the min and max curves of HVSRN. The curves are plotted in the frequency range 0.1-20 Hz in order to fully illustrate the frequency peaks (peaks and troughs).

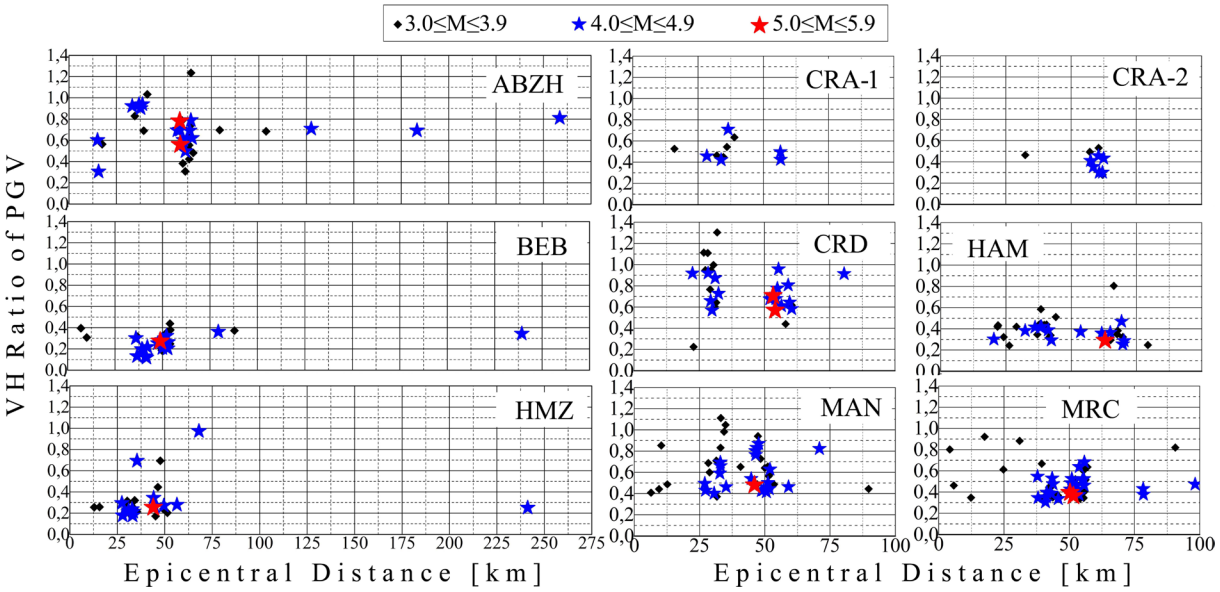

Figure 6. The VH ratio of PGV variation with the epicentral distance and Mw classes (3.0-3.9, 4.0-4.9, and 5.0-5.9) of the seismic events recorded by each station of Fig. 2b.

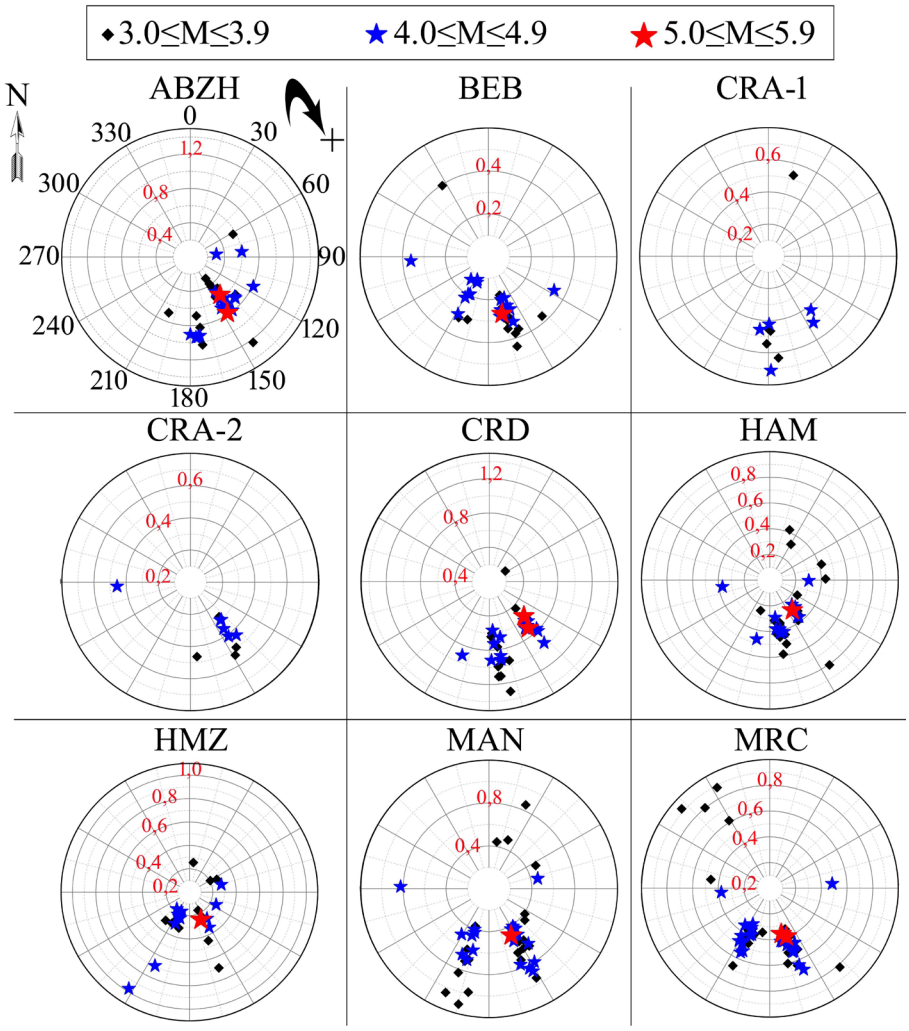

Figure 7. The VH ratio of PGV variation with azimuth angle and Mw classes (3.0-3.9, 4.0-4.9, and 5.0-5.9) of the seismic events recorded by each station of Fig. 2b. The VH ratios of PGV are mentioned in red on circle grids.

ratios of the PGV has no correlation with the magnitude class, in all cases of station and epicentral distance (Fig. 6). Therefore, the comparison of the observed VH ratio of PGV variation between stations showed that the stations BEB and HMZ of S2 soil classification have the majority of VH ratios below 0.4, whereas for the rest of the stations of the S1 soil classification, most ratios are greater than 0.4 (Fig. 3c and 3d, Table 5).

The VH ratio of PGV variation with azimuth is shown in Fig. 7, which shows that the majority of our data set used contains aftershocks from the Hammam-Melouane and Mihoub regions (rectangles numbered 2 and 3 in Fig. 1b, respectively). The illustration in Fig. 7 shows variations in VH ratio, which well observed at all the stations.

The results of the linear fitting obtained in the present study using the observed VH ratio of PGV for the S1-irregular and S1-flat surface categories are illustrated in Fig. 8 with the corresponding residuals, a simple difference between the observed and the fitted VH ratios of PGV. Both linear fittings have the same trend of decreasing with R_{JB}, and there is very little variation from 0.60 to 0.55 for distances from 20 to 70 km. This suggests that the topography does not influence the variation in the VH ratio of PGV. In Fig. 9a, the linear fitting obtained is plotted considering all observed VH ratios of PGV of the S1 soil classification (Table 5), while Fig. 9b shows the linear fitting obtained for the observed VH ratio of PGV in S2 soil classification (Table 5). The two obtained linear fittings are compared to the predictors AA2014, BC2016, and RA2021 considering the case of Mw = 4.5 and Vs30 = 1030 m/s for S1 and 400 m/s for S2. The value of Mw = 4.5 was considered as the average value for the range of magnitudes of our seismic event dataset in this study. The value of Vs30 = 1030 m/s for S1 was considered according to the JICA project (2006), and Vs30 = 400 m/s for S2 is an average value from boreholes near the BEB and HMZ stations (Laouami, 2020). For S1, an opposite trend was observed between the linear fitting and the predictors (Fig. 9a). The large number of observations (Fig. 3c) with a VH ratio <0.6 (R_{JB} between 50 and 70 km) may be the cause of this inverse trend. On the other hand, the linear fitting shows the same trend as the predictors in the case of soil class S2 (Fig. 9b). All show a slight increase with distance.

According to Fig. 9a, the linear fitting obtained for S1 shows a slightly different variation trend with R_{JB}. Comparison of this obtained linear fitting with the selected predictors shows that the latter are in close proximity, with variations from 0.50 to 0.75 depending on the R_{JB}, and with the VH ratio of PGV modeled using the RA2021 predictor being the nearest. For S1 soil classification, it appears that all three predictors provide broadly similar trends (Fig. 9a). According to Fig. 9a, the linear fitting obtained and the three predictors vary around 0.6 with

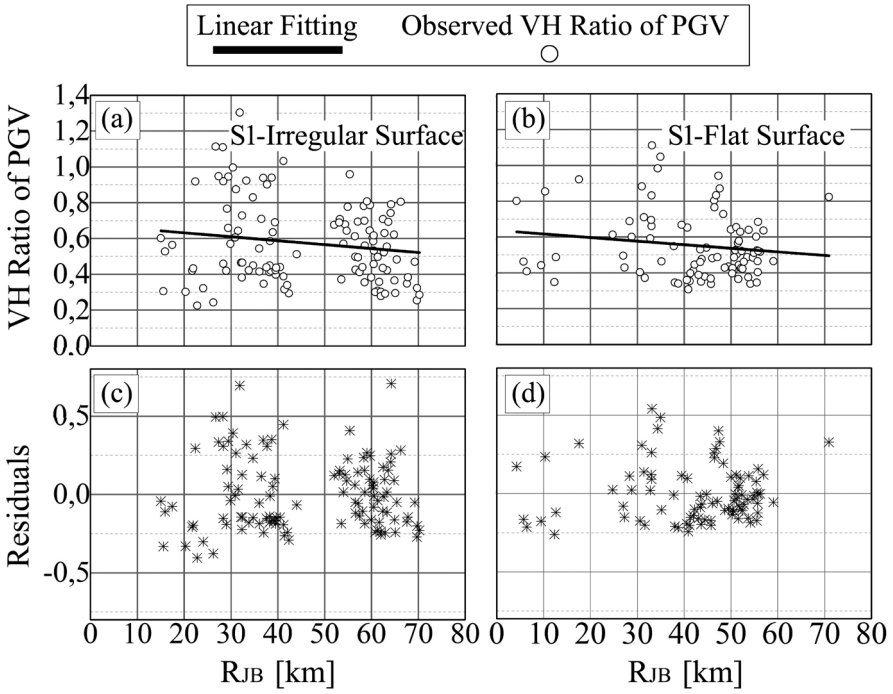

Figure 8. Top panels show the linear fitting (black lines) obtained in the present study considering the observed VH ratios of PGV (unfilled circles) at (a) S1 soil classification of irregular surface, and (b) S1 soil classification of flat surface. Bottom panels (c and d) are the corresponding residuals of the linear fittings from the observed VH ratios of PGV in (a) and (b), respectively.

a slight variation with R_{JB}, where in general the vertical PGV is equal to half plus a small factor "a" of the horizontal PGV ($PGV_V = 0.5 * PGV_H + a * PGV_H$; where $a < 0.2$) (Fig. 9a). At this point, we can say that all three predictors are suitable for classifying S1 soils for the R_{JB} up to 70 km.

For the linear fitting obtained for S2 soil classification, a similar trend with the selected predictors is observed, but with a larger offset (Fig. 9b). Therefore, this result is not surprising because the two considered stations, BEB and HMZ, were installed in an area of strong site-effects observed during the 2003 Boumerdès earthquake (Mw = 6.9) at the Dar-el-Beida (DB) Algerian accelerograph station (Laouami et al., 2006; Meslem et al., 2010). The largest PGV

Table 6. Recorded PGV [cm/s] of the 2003 Boumerdès earthquake at the three stations of Algerian accelerograph network on the EW, NS, and vertical components, the corresponding fundamental frequency, f_0 [Hz] (Laouami et al., 2006), and the observed VH ratio. The f_0 of Hussein-Dey and Kouba stations are according to Meslem et al. (2010). The DB, HD, and KB code locations are given in Fig. 2a.

Station	East-West	North-South	Vertical	f_0	VH ratio of PGV
Dar-el-Beida (DB)	27.5	40.6	10.7	3.4	0.31
Hussein-Dey (HD)	16.5	9.1	7.7	6.6	0.58
Kouba (KB)	10.5	13.7	6.5	10	0.53

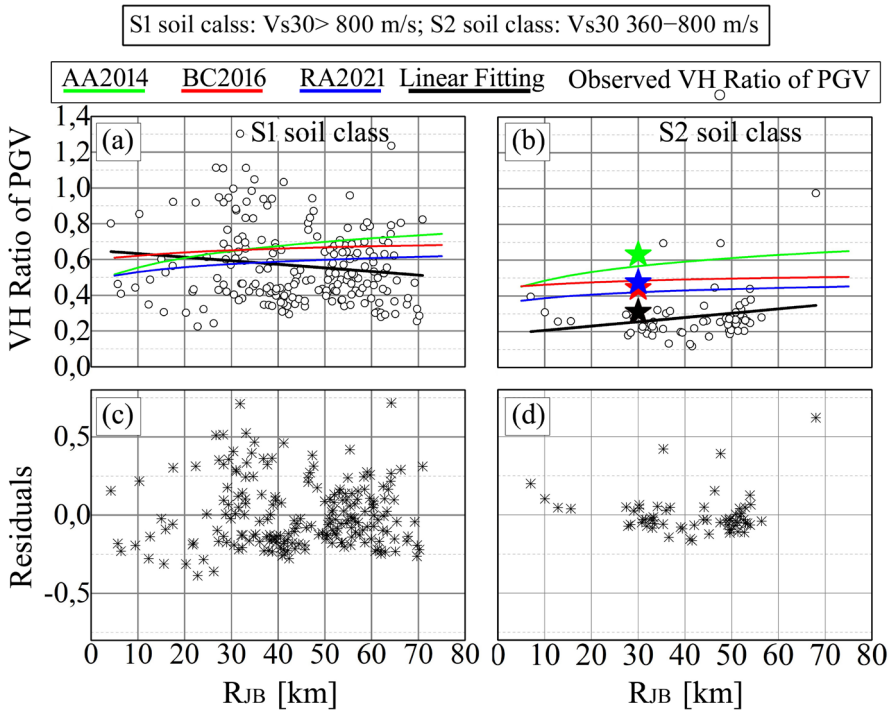

Figure 9. Top panels show the linear fitting (black lines) obtained in the present study considering the observed VH ratios of PGV (unfilled circles) from (a) S1 and (b) S2 soil classifications, compared to the predictors of Akkar et al. (2014) (AA2014), Bozorgnia and Campbell (2016) (BC2016), Ramadan et al. (2021) (RA2021). In the computation of the modeled VH ratios of PGV from AA2014, BC2016, and RA2021 predictors, the Vs30 was considered equal to 1030 m/s in S1, 400 m/s in S2, and Mw = 4.5. Black star in (b) is the observed VH ratios of PGV at Dar-el-Beida station from the 2003 Boumerdès earthquake mainshock recording. Green, red, and blue stars are the modeled VH ratios using AA2014, BC2016, and RA2021 predictors respectively (Mw = 6.8, R_{JB} = 30 km, and Vs30 = 400 m/s). Bottom panels (c and d) are the corresponding residuals of the linear fittings from the observed VH ratios of PGV in (a) and (b).

of the mainshock of this earthquake was recorded at the Dar-el-Beida station on the NS component (Table 6) in comparison with the Hussein-Dey and Kouba stations (Laouami et al., 2006). According to Meslem et al. (2010), the ground motion at the Dar-el-Beida station was strongly affected by the local soil conditions, and Laouami et al. (2006) explained this phenomenon by a correlation between its f_0 (3.4 Hz) and the predominant frequency of the earthquake (3 Hz). For these three stations, in Table 6, there is a presentation of the recorded PGV on each component, f_0, and the corresponding VH (Laouami et al., 2006; Meslem et al., 2010). In Fig. 9b, the VH ratio of PGV at the Dar-el-Beida station (0.31) at 30 km from the epicenter is illustrated in black star. The VH ratio of PGV of the 2003 Boumerdès earthquake at this station has a value less than 0.4, in correlation with the majority of the observed VH ratios from Fig. 3d, which are moderate-to-low magnitude. Based on the results of Meslem et al. (2010), this may be explained by the absence of a nonlinear soil behavior from the slightly and insignificant increasing of PGV with the estimated f_0 of the mentioned three accelerograph stations using 14 weak and strong ground motions in the HVSRN technique.

We considered the same parameters of the 2003 Boumerdès earthquake (Mw = 6.9, R_{JB} = 30 km, and Vs30 = 400 m/s) in the three selected predictors for VH ratio of PGV computation and comparison with the observed one. The obtained results are shown in Fig. 9b (colored stars), and one can say that the selected predictors overestimate the VH ratio of PGV in comparison with the observed one at the Dar-el-Beida station (black star); this is not because the PGV in the vertical component is small, but because the horizontal one is more important. Moreover, more factors, such as the impedance contrast and f_0 can contribute to the site response amplification. In such case of amplification, Fig. 10 shows the observed VH ratios of the 5% damping acceleration response spectra (SA) at the Dar-el-Beida and Hussein-Dey stations of the mainshock recording of the 2003 Boumerdès earthquake (Mw = 6.9) (Fig. 1a and 2a). Both sites present maxima at 0.06 (0.91) and 2.4 (0.89) sec at Dar-el-Beida and Hussein-Dey stations, respectively.

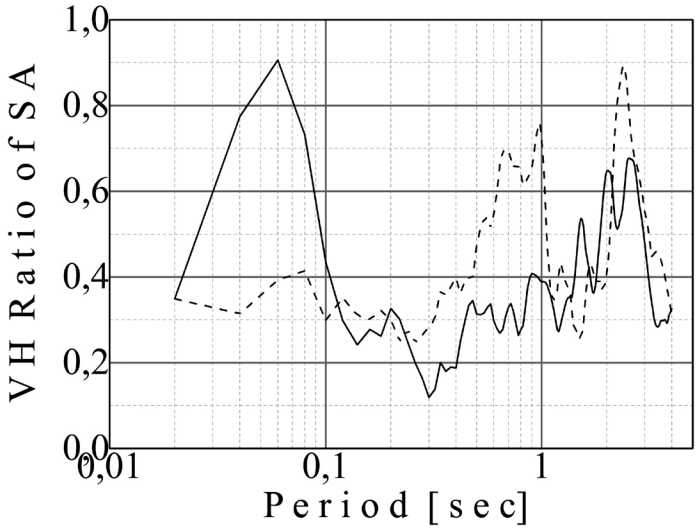

Figure 10. The observed VH ratio of the 5% damping acceleration response spectra (SA) at Dar-el-Beida (continued line) and Hussein-Dey (dashed line) Algerian accelerograph stations from the 2003 Boumerdès earthquake (Mw = 6.9) recordings.

Despite the significant lithological site-effects in the study area, and the comparison between the linear fitting and the three predictors leads to the conclusion that the RA2021 model is the most reasonable for the classification of S2 soils in our study area, where the VH ratio of PGV varies around 0.4 according to Fig. 9b.

In order to refine the selection of the best predictors for S1 and S2 in this comparative analysis, we used in addition the Euclidean Distance-based Ranking method (EDR) proposed by Kale and Akkar (2013). The authors encourage the utilization of this method as a tool in ranking several candidate GMPEs for probabilistic seismic hazard assessment, based on two individual or combined components of EDR, the uncertainty in ground motion estimations (aleatory variability addressed by the standard deviation, or sigma), and the trend between the observed and estimated data (model bias). The performance of each candidate GMPE is tested by the separate or the combination of the aleatory variability and the model bias. These two components are given by the Modified Euclidean Distance normalized by

the number of the observed data, N, (MDE_norm), and the square root of the κ parameter. The MDE_norm and κ are given by the equations n° 6 and 9a in Kale and Akkar (2013). The combination of these two components gives the third parameter, EDR value, defined in the equation n° 11 in Kale and Akkar (2013), where its smaller value is an indicator of a best representation of the observed data by the predictive model (Kale and Akkar, 2013).

In our case, the application of EDR method was performed considering the three candidate predictors of AA2014, BC2016, and RA2021 and the observed VH ratio of PGV for S1 and S2 soil classes for epicentral distance less than 75 km (Fig. 3). In the computation of MDE_norm, $\sqrt{\kappa}$, and EDR value, we used the MATLAB program of Kale and Akkar (2013), and the obtained results are presented in Table 7. According to this comparison, it is shown that the RA2021 predictor provided the smaller value in MDE_norm for the two soil classes, where the AA2014 predictor gave smaller value in $\sqrt{\kappa}$, for the two soil classes (Table 7). These results can be interpreted as a small sigma between our observed VH ratios of PGV and the estimated ones using the RA2021 predictor, and a good trend when using the AA2014 predictor. For each case of candidate predictors, the combination of sigma and the trend (MDE_norm and $\sqrt{\kappa}$, respectively) provided smaller EDR values in AA2014 for S1 and RA2021 for S2 (Table 7). For BC2016 predictor, larger values were obtained for the individuals' components separately, and their combination (Table 7). This can be explained by the complex predictor parameters used in BC2016 in comparison with AA2014 and RA2021, demonstrated previously by Kale and Akkar (2013).

Table 7. Results of comparison between the candidate predictors of VH ratio of PGV and the observed ones using the Euclidean distance-based (EDR) ranking method (Kale and Akkar, 2013). In this comparison, the Vs30 parameter is used from the RPA code (2024) of the two soil classes, S1 and S2, in our study area. The results are the Modified Euclidean Distance, MDE_norm, normalized by N, the square root of Kappa, $\sqrt{\kappa}$, and the EDR value. The number N of the observed VH ratio of PGV is 205 for S1, and 63 for S2, with epicentral distance less than 75 km. In bold, it is selected the smaller values in each case.

Predictors	S1 soil class (rock soil Vs30 >800 m/s)			S2 soil class (stiff soil, Vs30: 360-800 m/s)		
	MDE_norm	$\sqrt{\kappa}$	EDR	MDE_norm	$\sqrt{\kappa}$	EDR
AA2014	0.49	**2.63**	**1.31**	0.88	**3.88**	3.44
BC2016	0.51	4.00	2.04	0.74	5.59	4.18
RA2021	**0.40**	3.33	1.36	**0.61**	4.42	**2.71**

The AA2014 and RA2021 models are the most suitable predictors for the VH ratio of the PGV estimate for soil class S1, as shown in Fig. 9a, which presents the computation and comparison of linear fitting. This result is also confirmed by Table 7, which gives the results of the EDR method. The RA2021 predictor seems to be the most appropriate for such an estimation for soil class S2, despite the presence of significant lithological site-effects in the study area.

As mentioned earlier in the Introduction section, knowing the ratio between the horizontal and vertical components makes it possible to measure the extent to which the vertical component contributes to the resistance of a structure and its foundations against inertial loading. Based on the observation that the RA2021 predictor is one of the best suited to soil classes S1 and S2 for R_{JB} up to 70 km (Fig. 9 and Table 7), we provide in Tables 8 and 9 the estimated VH ratios of PGV, considering different seismic scenarios in terms of Mw (3.5, 4.5, and 5.3) and R_{JB} (20, 30, 40, 50, and 60 km).

The selection of Mw and R_{JB} ranges is in good agreement with our used seismic data and finding. For this analysis, we considered three Vs30 values for S1 soil class, 800, 1000 and 1500 m/s, and 400, 500 and 600 m/s for S2, according to the RPA code (2024) (Table 2). The results presented in Table 8 and 9 can assist engineering design by providing an initial estimate of the relative ratio between the horizontal and vertical components of PGV. As previously mentioned, the site's Vs30 has the greatest influence on the VH ratio of PGV, surpassing the effects of Mw and R_{JB} variations. According to Table 8, the mean VH ratios of PGV for Vs30 values of 800, 1000, and 1500 m/s are 0.54, 0.58 and 0.66, respectively. Table 9 shows mean VH ratios of 0.42, 0.45, and 0.48 for Vs30 values of 400, 500, and 600 m/s, respectively.

Table 8. Estimated VH ratios of PGV for different Vs30 of rock soil class (S1) from the RPA code (2024), considering different seismic scenarios in term of Mw and R_{JB}, obtained from the RA2021 predictor (Ramadan et al., 2021), for a direct application in engineering design.

Vs30 = 800 m/s									
Mw	R_{JB} (km)								
	20	25	30	35	40	45	50	55	60
3.5	0.48	0.49	0.50	0.51	0.51	0.52	0.52	0.53	0.53
4.5	0.51	0.52	0.53	0.53	0.54	0.55	0.55	0.55	0.56
4.8	0.52	0.53	0.54	0.54	0.55	0.55	0.56	0.56	0.57
5.0	0.53	0.53	0.54	0.55	0.55	0.56	0.56	0.57	0.57
5.3	0.53	0.54	0.55	0.56	0.56	0.57	0.57	0.58	0.58

Vs30 = 1000 m/s									
Mw	R_{JB} (km)								
	20	25	30	35	40	45	50	55	60
3.5	0.52	0.53	0.54	0.55	0.55	0.56	0.56	0.57	0.57
4.5	0.55	0.56	0.57	0.58	0.58	0.59	0.59	0.60	0.60
4.8	0.56	0.57	0.58	0.58	0.59	0.60	0.60	0.61	0.61
5.0	0.57	0.58	0.58	0.59	0.60	0.60	0.61	0.61	0.62
5.3	0.58	0.59	0.59	0.60	0.61	0.61	0.62	0.62	0.63

Vs30 = 1500 m/s									
Mw	R_{JB} (km)								
	20	25	30	35	40	45	50	55	60
3.5	0.60	0.61	0.62	0.62	0.63	0.64	0.64	0.65	0.65
4.5	0.63	0.64	0.65	0.66	0.67	0.67	0.68	0.68	0.69
4.8	0.64	0.65	0.66	0.67	0.68	0.68	0.69	0.69	0.70
5.0	0.65	0.66	0.67	0.68	0.68	0.69	0.69	0.70	0.70
5.3	0.66	0.67	0.68	0.69	0.69	0.70	0.71	0.71	0.72

Table 9. Estimated VH ratios of PGV for different Vs30 of stiff soil class (S2) from the RPA code (2024), considering different seismic scenarios in term of Mw and R_{JB}, obtained from the RA2021 predictor (Ramadan et al., 2021), for a direct application in engineering design.

Vs30 = 400 m/s									
Mw	R_{JB} (km)								
	20	25	30	35	40	45	50	55	60
3.5	0.38	0.39	0.39	0.40	0.40	0.41	0.41	0.41	0.42
4.5	0.40	0.41	0.42	0.42	0.43	0.43	0.43	0.44	0.44
4.8	0.41	0.42	0.42	0.43	0.43	0.44	0.44	0.44	0.45
5.0	0.41	0.42	0.43	0.43	0.44	0.44	0.45	0.45	0.45
5.3	0.42	0.43	0.43	0.44	0.44	0.45	0.45	0.45	0.46

Vs30 = 500 m/s									
Mw	R_{JB} (km)								
	20	25	30	35	40	45	50	55	60
3.5	0.41	0.42	0.42	0.43	0.43	0.44	0.44	0.45	0.45
4.5	0.43	0.46	0.45	0.45	0.46	0.46	0.47	0.47	0.47
4.8	0.44	0.45	0.45	0.46	0.47	0.47	0.47	0.48	0.48
5.0	0.45	0.45	0.46	0.47	0.47	0.47	0.48	0.48	0.49
5.3	0.45	0.46	0.47	0.47	0.48	0.48	0.49	0.49	0.49

Vs30 = 600 m/s									
Mw	R_{JB} (km)								
	20	25	30	35	40	45	50	55	60
3.5	0.44	0.44	0.45	0.46	0.46	0.47	0.47	0.47	0.48
4.5	0.46	0.47	0.48	0.48	0.49	0.49	0.50	0.50	0.50
4.8	0.47	0.48	0.48	0.49	0.49	0.50	0.50	0.51	0.51
5.0	0.47	0.48	0.49	0.49	0.50	0.50	0.51	0.51	0.52
5.3	0.48	0.49	0.50	0.50	0.51	0.51	0.52	0.52	0.52

In addition, we estimated the far field VH ratio of PGV using the AA2014, BC2016, RA2021, and ZD2019 predictors for three strong earthquake magnitudes, 6.5, 7.0 and 7.5. These magnitudes correspond to known seismic activity in Algeria, such as the 1980 El-Asnam earthquake (M7.3) and the 2003 Boumerdès earthquake (M6.9). The far-field VH of PGV was computed for four soil classes according to the RPA code (2024) (Table 2). Figure 11 displays the estimated VH ratios of PGV for Mw = 6.5, 7.0, and 7.5 across each soil class with corresponding Vs30 values. This analysis considers a reverse fault mechanism. Note that the ZD2019 predictor estimates VH ratios only for, S1, S2, S3 soil classes. The results shown in Fig. 11 illustrate how the far-field VH ratio of PGV varies with R_{JB} and soil class, serving as an initial quantification of vertical ground motion relative to horizontal motion. According to AA2014, RA2021, and ZD2019 predictors, rock soils can produce a VH ratio around 0.85, indicating vertical PGV close to horizontal PGV, whereas BC2016 predicts a ratio around 0.6, similar to near-field conditions shown in Fig. 4. The influence of earthquake magnitude on the VH ratio of PGV is negligible across all four soil classes, based on results from AA2014, BC2016 and RA2021 predictors.

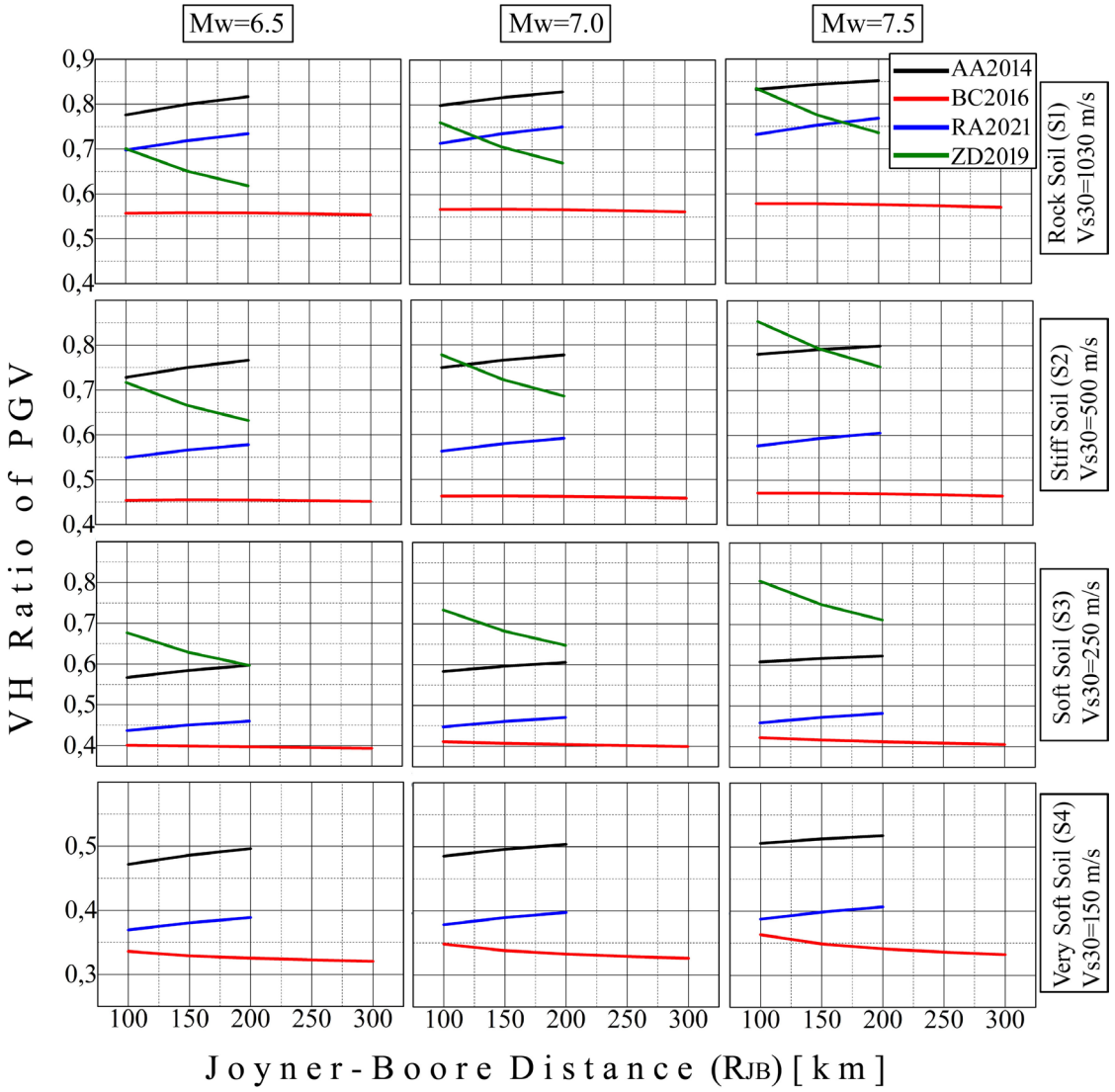

Figure 11. Estimated VH ratio of PGV for far-filed using the four predictors, AA2014, BC2016, RA2021, and ZD2019 (Table 1) for three Mw values, 6.5, 7.0, and 7.5, for different soil classes and Vs30, according to the RPA code (2024) (Table 2).

In the present study, the PGV is associated with the surface-wave, the strongest seismic phase, because our seismic dataset is composed of relatively earthquakes from epicentral distance between 30 and 80 km (He et al., 2023). In this case, the soil conditions play a major role in modifying the peak-ground parameters and the frequency content of a seismic event through amplification. During an earthquake, surface waves (Rayleigh and Love waves)

have a rich low-frequency content and long duration, which makes them more destructive than body waves (P and S waves). In a 1-D model of a sediment layer overlying bedrock, the impedance contrast between them is the source of these modifications in a seismic record. According to Bonnefoy-Claudet (2004), this impedance contrast has an impact on the fundamental mode of Rayleigh-wave ellipticity, the soil frequency, and the frequency peak of the HVSRN curve. At the boundaries of sedimentary basins, surface waves can cause significantly stronger damage than the 1-D effect due to predominantly constructive interference between body and surface waves, which is typically considered a 2-D vertical cross-section effect (Kawase, 1996). According to Bowden and Tsai (2017), accounting for surface-wave amplification in seismic-hazard characterization is essential for accurately predicting strong ground motion. Perraud et al. (2022) examined the effect of Rayleigh waves on the seismic response of bridge pylons to assess the additional distress they cause and to determine possible correlations with their frequency content. According to the same authors, many design standards and practical guidelines do not explicitly consider the presence or effects of surface waves.

6. Conclusion

In this study, we analyzed 285 vertical-to-horizontal (VH) ratios of peak ground velocity (PGV) recorded during weak to moderate earthquakes, collected from seismic stations installed in the Bay of Algiers, on the flat surface of the Mitidja Basin, and on the sloping terrain of the Bouzaréah Massif, characterized by rocky and stiff soils. Our analysis included linear fitting computations and comparisons with VH ratios of PGV predicted by models available in the literature. In addition, the Euclidean Distance-based ranking method (EDR) was applied to rank the degree of performance of each candidate predictor, measuring the sigma and the trend between the estimated and observed VH ratio of PGV. With regard to rocky soils, our results indicated that all the models provide a satisfactory approximation of the observed VH ratio of PGV. These models correspond well to our linear fitting calculated for distances (R_{JB}) up to 70 km. The modeled VH ratio of PGV for rocky soil is approximately 0.6. For stiff soil, it was challenging to identify a suitable predictor for the study area due to the significant site-effects observed at the seismic stations. These site-effects, confirmed by previous studies, resulted in a minimum difference of about 0.1 and 0.2 between our computed VH ratio of PGV and the lowest predictor (Ramadan et al., 2021). Despite this local phenomenon, we admit that the predictor suggested by Ramadan et al. (2021) provides a reasonable fit. The modeled VH ratio of PGV has a variation around 0.4.

In the present study, the use of the point-source model in our comparative analysis has clear limitations, as the R_{JB} distance is assumed to be equivalent to the epicentral distance. This simplification neglects complexities such as rupture directivity, spatial variation in slip, and other finite-fault effects. To develop a region-specific predictor, further research on VH ratios of PGV is needed by collecting additional data, developing more sophisticated local models, or incorporating more detailed topographical and geological factors into the predictors, in order to draw more definitive conclusions.

In the RPA code (2024), there is no recommendation regarding vertical motion in terms of ground-motion parameters (PGA, PGV, or SA) for foundation-uplift assessments. In many seismic-microzonation projects carried out for Algerian cities exposed to high seismic risk, vertical motion is not considered at all. In the Bay of Algiers, we showed that the most important seismological parameter controlling the VH ratio of PGV is Vs30 (soil type), with the vertical PGV generally being about half of the horizontal PGV for rock sites. Despite the low VH ratio of PGV for S2 stiff soil, this does not imply that vertical motion has a negligible role in increasing the risk of damage, as confirmed by the observed VH ratio of SA at Dar-el-Beida. Therefore, it is recommended to include the VH ratio of ground-motion parameters in seismic-design applications, at least for particular categories of buildings.

Data and sharing resources. Seismograms used in this study were provided by the Algerian Digital Seismic Network (ADSN) of the Astronomy, Astrophysics and Geophysics Research Center, Algeria (CRAAG) (last accessed October 2021).
Plots were made using the Generic Mapping Tools version 5.4.5.
Computations were made using Matlab.

Data availability statement. The datasets analyzed during the current study are not publicly available because they have not yet been made public but are available from the corresponding author on reasonable request.

Acknowledgements. The authors wish to express their gratitude to the Editor-in-Chief, Professor Paola Montone, and the Sector Editor, Dr. Ester Piegari, for their consideration of our work and their management of the review process. We also extend our sincere thanks to the three anonymous reviewers for their constructive comments and recommendations, which significantly enhanced the manuscript. We would like thank the staff of ADSN-CRAAG for providing the earthquake data recorded by the temporary seismic network installed in the Bay of Algiers. We also thank the CGS for supplying data related to the mainshock of the 2003 Boumerdès earthquake. Our gratitude goes to Dr. Nasser Laouami of CGS-Algeria for providing the code used in the present study. The authors thank Dr. Özkan Kale and Dr. Sinan Akkar for generously sharing their Matlab code for the Euclidean distance-based ranking method for research purposes. We equally appreciate Dr. Mohamed Khelif for his valuable discussions regarding the temporary seismic network and earthquake data. Prof. Dr. Stefano Parolai and Dr. Shahabaldin Mazloom are gratefully acknowledged for their insightful discussions and suggestions.

References

Akkar, S. and J. J. Bommer (2007). Empirical prediction equations for peak ground velocity derived from strong-motion records from Europe and the Middle East, Bull. Seismol. Soc. Am., 97, 2, 511-530, doi:10.1785/0120060141.

Akkar, S. and Ö. Özen (2005). Effect of peak ground velocity on deformation demands for SDOF systems, Earthq. Eng. Struct. Dyn., 34, 1551-1571, doi:10.1002/eqe.492.

Ambraseys, N. N. and J. Douglas (2003). Near-field horizontal and vertical earthquake ground motions, Soil Dyn. Earthq. Eng., 23, 1, 1-18, doi:10.1016/S0267-7261(02)00153-7.

Anbazhagan, P., A. Kumar and T. G. Sitharam (2013). Ground motion prediction equation considering combined dataset of recorded and simulated ground motions, Soil Dyn. Earthq. Eng., 53, 92-108, doi:10.1016/j.soildyn.2013.06.003.

Atkinson, G. M., D. M. Boore, K. Assatourians, K. W. Campbell et al. (2009). A guide to differences between stochastic point-source and stochastic finite-fault simulations, Bull. Seismol. Soc. Am., 99, 3192-3201, doi:10.1785/0120090058.

Benfedda, A., K. Abbes, D. Bouziane, Y. Bouhadad et al. (2017). The August 1st, 2014 (Mw 5.3) moderate earthquake: Evidence for an active thrust fault in the Bay of Algiers (Algeria), Pure Appl. Geophys., 174, 1503-1511, doi:10.1007/s00024-017-1481-6.

Benjamin, E., B. Zurek, E. Dedem, P. Stafford et al. (2019). Simulations for the development of a ground-motion model for induced seismicity in the Groningen gas field, The Netherlands, Bull. Earthq. Eng., 17, 4441-4456, doi:10.1007/s10518-018-0479-5.

Bommer, J. J., S. Akkar and Ö. Kale (2011). A model for vertical-to-horizontal response spectral ratios for Europe and the Middle East, Bull. Seismol. Soc. Am., 101, 4, 1783-1806, doi:10.1785/0120100285.

Bommer, J. and J. E. Alarcón (2006). The prediction and use of peak ground velocity, J. Earthq. Eng., 10, 1, 1-31, doi:10.1080/13632460609350586.

Bonnefoy-Claudet, S. (2004). Utilisation combinée des méthodes basées sur le bruit de fond dans le cadre du microzonage sismique, PhD thesis, Univ. Joseph Fourier, Grenoble, France.

Bozorgnia, Y. and K. W. Campbell (2016). Ground motion model for the vertical-to-horizontal (V/H) ratios of PGA, PGV, and response spectra, Earthq. Spectra, 32, 951-978, doi:10.1193/100614eqs151m.

Bureau de Recherches Géologiques et Minières (2005). Étude de réduction de la vulnérabilité du massif de Bouzaréah aux catastrophes naturelles, Report ISL R3016.doc, BRGM/RC-53909-FR.

Campbell, K. W. and Y. Bozorgnia (2014). NGA-West2 Campbell-Bozorgnia ground-motion model for the horizontal components of PGA, PGV, and 5%-damped elastic pseudo-acceleration response spectra, Earthq. Spectra, 30, 1087-1115, doi:10.1193/062913EQS175m.

Chen, C. T., S. C. Chang and K. L. Wen (2017). Stochastic ground-motion simulation of the 2016 Meinong, Taiwan earthquake, Earth Planets Space, 69, 62, doi:10.1186/s40623-017-0645-z.

Chieffo, N., M. Marius, A. Formisano, P. B. Lourenço et al. (2021). The effect of ground-motion vertical component on the seismic response of historical masonry buildings, Eng. Struct., 249, 113346, doi:10.1016/j.engstruct.2021.113346.

Clinton, J. F. and T. H. Heaton (2002). The potential advantages of a strong-motion velocity meter over a strong-motion accelerometer, Seismol. Res. Lett., 73, 332-342, doi:10.1785/gssrl.73.3.332.

Bowden, D. C. and V. C. Tsai (2017). Earthquake ground-motion amplification for surface waves, Geophys. Res. Lett., 44, 121-127, doi:10.1002/2016GL071885.

Derras, B., P. Y. Bard, J. Régnier and H. Cadet (2020). Nonlinear modulation of site response, Eng. Geol., 269, 105500, doi:10.1016/j.enggeo.2020.105500.

Derrich, Z. and G. Cheikh-Lounis (2004). Geotechnical characteristics of the Plaisancian marls of Algiers, Bull. Eng. Geol. Environ., 63, 367-378, doi:10.1007/s10064-004-0246-5.

Duofa, J., L. Chenxi and Z. Changhai (2025). Wave-propagation modeling using a machine-learning-based finite-difference scheme, J. Comput. Phys., 529, 113870, doi:10.1016/j.jcp.2025.113870.

Gherboudj, F., N. Mezouar, T. Ouzandja and Y. Bouhadad (2024). Probabilistic seismic hazard maps and uniform hazard spectra with site-effect integration for northern Algiers, Nat. Hazards, 120, 7653-7677, doi:10.1007/s11069-024-06502-7.

Gülerce, Z. and N. A. Abrahamson (2011). Site-specific design spectra for vertical ground motion, Earthq. Spectra, 27, 4, 1023-1047, doi:10.1193/1.3651317.

Hallal, N., A. Yelles-Chaouche, L. Hamai, A. Lamali et al. (2019). Spatiotemporal evolution of the El Biar landslide (Algiers), Bull. Eng. Geol. Environ., 78, 5653-5670, doi:10.1007/s10064-019-01492-4.

Hartzell, S., M. Meremonte, L. Ramírez-Guzmán and D. McNamara (2014). Ground motion in the presence of complex topography, Bull. Seismol. Soc. Am., 104, 451-466, doi:10.1785/0120130088.

He, X., P. Zhang, S. Ni, R. Chu et al. (2023). Automatic determination of focal depth with the optimal period of Rayleigh wave amplitude spectra, Geophys. J. Int., 235, 1681-1696, doi:10.1093/gji/ggad326.

Heddar, A., C. Authemayou, H. Djellit, A. K. Yelles et al. (2013). Preliminary results of a paleoseismological analysis along the Sahel fault (Algeria), Quat. Int., 302, 210-223, doi:10.1016/j.quaint.2012.09.007.

Issaadi, A., A. Saadi, F. Semmane and A. Yelles-Chaouche (2020). Liquefaction potential and Vs30 structure in the Middle-Chelif Basin, Appl. Sci., 12, 8069, doi:10.3390/app12168069.

Japan International Cooperation Agency (2006). A study of seismic microzoning of the Wilaya of Algiers, Final Report, 2, Oyo Int. Corp. and Nippon Koei Co., Ltd.

Kaklamanos, J., L. G. Baise and D. M. Boore (2011). Estimating unknown input parameters when implementing the NGA ground-motion prediction equations, Earthq. Spectra, 27, 1219-1235, doi:10.1193/1.3650372.

Karimzadeh, S., A. Mohammadi, U. Salahuddin, A. Carvalho et al. (2024). Backbone ground-motion model through simulated records and XGBoost machine-learning algorithm, Earthq. Eng. Struct. Dyn., 53, 668-693, doi:10.1002/eqe.4040.

Kawase, H. (1996). The cause of the damage belt in Kobe, Seismol. Res. Lett., 67, 25-34, doi:10.1785/gssrl.67.5.25.

Khelif, M. F., A. Yelles-Chaouche, Z. Benaissa, F. Semmane et al. (2018). The 2016 Mihoub earthquake sequence, Tectonophysics, 736, 62-74, doi:10.1016/j.tecto.2018.03.015.

Kherroubi, A., J. Déverchère, A. Yelles, B. Mercier de Lépinay et al. (2009). Recent and active deformation pattern off the easternmost Algerian margin, Mar. Geol., 261, 17-32, doi:10.1016/j.margeo.2008.05.016.

Konno, K. and T. Ohmachi (1998). Ground-motion characteristics estimated from spectral ratio between horizontal and vertical components of microtremor, Bull. Seismol. Soc. Am., 88, 228-241, doi:10.1785/BSSA0880010228.

Laouami, N. (2019). Vertical ground-motion prediction equations and vertical-to-horizontal ratios for Algeria, Bull. Earthq. Eng., 17, 3637-3660, doi:10.1007/s10518-019-00635-y.

Laouami, N., N. Slimani, Y. Bouhadad, J. L. Chatelain and A. Nour (2006). Evidence for fault-related directionality and localized site effects from the 2003 Boumerdès earthquake, Soil Dyn. Earthq. Eng., 26, 991-1003, doi:10.1016/j.soildyn.2006.03.006.

Laouami, N. (2020). Proposal for a new site-classification tool using microtremor data, Bull. Earthq. Eng., 18, 2A, doi:10.1007/s10518-020-00882-4.

Layadi, K., F. Semmane and A. K. Yelles-Chaouche (2016). Site-effects investigation in the city of Chlef, Bull. Seismol. Soc. Am., 106, 2185-2196, doi:10.1785/0120150365.

Layadi, K., F. Semmane and A. K. Yelles-Chaouche (2022). Azimuth dependence in topographical site effects, Proc. 2nd Springer Conf. Arabian J. Geosci, Advances in Science, Technology and Innovation, Springer, Cham, 2, 217-220, doi:10.1007/978-3-030-73026-0_50.

Layadi, K., F. Semmane, A. Yelles-Chaouche, A. Saadi et al. (2023). Site characterization of Algerian broadband seismic stations, J. Seismol., 27, 45-75, doi:10.1007/s10950-022-10126-4.

Maouche, S. and A. Harbi (2018). The active faults of the Mitidja Basin, Euro-Mediterr. J. Environ. Integr., 3, 21, doi:10.1007/s41207-018-0061-1.

Massa, M., S. Barani and S. Lovati (2014). Overview of topographic effects based on experimental observations, Geophys. J. Int., 197, 1537-1550, doi:10.1093/gji/ggt341.

Mazloom, S. and R. Assi (2022). Estimate of V/H spectral-acceleration ratios for firm-soil sites in Eastern Canada, Soil Dyn. Earthq. Eng., 159, 107350, doi:10.1016/j.soildyn.2022.107350.

Meslem, A., F. Yamazaki, Y. Maruyama, D. Benouar et al. (2010). Site-response characteristics evaluated from strong-motion records of the 2003 Boumerdès earthquake, Earthq. Spectra, 26, 803-823, doi:10.1193/1.3459158.

Midorikawa, S., M. Matsuoka and K. Sakugawa (1994). Site effects on strong-motion records observed during the 1987 Chhiba-Ken-Toho-Oki earthquake, Proc. 9th Japan Earthq. Eng. Symp., E-085-E-090.

Miura, H., M. Matsuoka, C. Lozano, H. García et al. (2020). Site amplification models of peak ground acceleration and velocity for the Bogotá Basin, Proc. 17th World Conf. Earthq. Eng, Sendai, Japan.

Nakamura, Y. (1989). A method for dynamic characteristics estimation of subsurface using microtremor on the ground surface, Q. Rep. RTRI, 30, 25-30.

Newmark, N. M. and W. J. Hall (1978). Development of criteria for seismic review of selected nuclear power plants, NUREG/CR-0098, U. S. Nuclear Regulatory Commission.

Parolai, S., D. Bindi, M. Baumbach, H. Grosser et al. (2004). Comparison of different site-response estimation techniques using aftershocks of the 1999 Izmit earthquake, Bull. Seismol. Soc. Am., 94, 1096-1108, doi:10.1785/0120030086.

Pavlenko, V. A. and O. V. Pavlenko (2023). Stochastic simulation and development of the ground-motion prediction equation for the Baikal Rift Zone, Izv. Phys. Solid Earth, 59, 29-40, doi:10.1134/S1069351323010032.

Perraud, Y., C. T. Chatzigogos, K. C. Meza-Fajardo and P. Labbé (2022). Effect of Rayleigh waves on seismic response of bridge pylons, Soil Dyn. Earthq. Eng., 152, 107043, doi:10.1016/j.soildyn.2021.107043.

Peterson, J. (1993). Observations and modeling of seismic background noise, U. S. Geological Survey Open-File Report 93-322, doi:10.3133/ofr93322.

Ramadan, F., C. Smerzini, G. Lanzano and F. Pacor (2021). An empirical model for the vertical-to-horizontal spectral ratios for Italy, Earthq. Eng. Struct. Dyn., 50, 4121-4141, doi:10.1002/eqe.3548.

Roubeche, K. (2025). Local and duration magnitude scales for northern Algeria based on local earthquake data (2010-2022), PhD thesis, Univ. Sétif, Algeria.

RPA (2024). Algerian seismic code, Ministry of Housing and Urban Planning, Algeria.

Saadi, A., A. Issaadi, F. Semmane, A. Yelles-Chaouche et al. (2023). 3D shear-wave velocity structure for Oran city, Soil Dyn. Earthq. Eng., 164, 107570, doi:10.1016/j.soildyn.2022.10757.

Semmane, F., B. Y. N. Benabdeloued and H. Beldjoudi (2015). The 22 February 2014 Mw 4.1 Bordj-Menaïel earthquake, Seismol. Res. Lett., 86, 794-802, doi:10.1785/0220140196.

Semmane, F., B. Y. N. Benabdeloued, A. Heddar and M. F. Khelif (2017). The 2014 Mihoub earthquake, J. Seismol., 21, 1385-1395, doi:10.1007/s10950-017-9671-3.

SESAME Project (2004). Guidelines for the implementation of the H/V spectral ratio technique on ambient vibrations, Deliverable D23.12, European Research Project EVG1-CT-2000-00026.

Seyhan, E. and J. P. Stewart (2014). Semi-empirical nonlinear site amplification from NGA-West2 data and simulations, Earthq. Spectra, 30, 1241-1256, doi:10.1193/063013EQS181M.

Silva, W. J. (1997). Characteristics of vertical strong ground motions for applications to engineering design, in I. M. Friedland, M. S. Power and R. L. Mayes (eds.), Proc. FHWA/NCEER Workshop on the National Representation of Seismic Ground Motion, Tech. Rep. NCEER-97-0010.

Tebbouche, M. Y., D. Ait Benamar, H. M. Hassan, A. P. Singh et al. (2022). Characterization of the El Kherba landslide triggered by the August 07, 2020, Mw 4.9 Mila earthquake, Environ. Earth Sci., 81, 46, doi:10.1007/s12665-022-10172-8.

Tebbouche, M. Y., D. Machane, S. Chabane, E. H. Oubaiche et al. (2017). Imagery of the metamorphic bedrock roof of the Sahel active fault, Arab. J. Geosci., 10, 292, doi:10.1007/s12517-017-3074-1.

Tsai, C. C. and H. W. Lui (2017). Amplification behavior of vertical motion observed from downhole arrays, in Proc. 16th World Conf. Earthq. Eng., Santiago, Chile.

Wathelet, M., J. L. Chatelain, C. Cornou and G. Di Giulio (2020). Geopsy: A user-friendly open-source tool set for ambient vibration processing, Seismol. Res. Lett., 91, 1878-1889, doi:10.1785/0220190360.

Xiao, Y. and M. Yamada (2022). XYtracker: A new approach to estimate fault rupture extent in real time for large earthquakes, Earth Planets Space, 74, 77, doi:10.1186/s40623-022-01650-1.

Yelles-Chaouche, A., T. Allili, A. Alili, W. Messemen et al. (2013). The new Algerian Digital Seismic Network (ADSN), Adv. Geosci., 36, 31-38, doi:10.5194/adgeo-36-31-2013.

Yelles-Chaouche, A., M. Khelif, A. Haned, A. Chami et al. (2018). The Algiers (north central Algeria) earthquake of August 1st, 2014 Mw 5.5 in the Algiers Bay tectonic context, J. Seismol., 23, 287-302, doi:10.1007/s10950-018-9806-1.

Zhang, B., X. Li, Y. Yu, J. Sun et al. (2023). A new ground-motion model for small-to-moderate earthquakes in the capital circle region of China, J. Asian Earth Sci., 257, 105853, doi:10.1016/j.jseaes.2023.105853.

Zolfaghari, M. R. and A. Darzi (2019). A prediction model for vertical-to-horizontal ratios of PGA, PGV, and 5%-damped response spectra for Iran, J. Seismol., 23, 4, 819-837, doi:10.1007/s10950-019-09836-z.

***CORRESPONDING AUTHOR: Khalissa LAYADI**,
Astronomy, Astrophysics and Geophysics Research Center, Algiers, Algeria
e-mail: khalissa.layadi@craag.edu.dz